Photon Flux Monitor for a Mono-energetic Gamma Ray Source

A Thesis Submitted to the College of
Graduate Studies and Research
in the Partial Fulfillment of the Requirements
for the Degree of Master of Science
in the
Department of Physics and Engineering Physics
University of Saskatchewan
Saskatoon

by

Octavian Mavrichi

Saskatoon, SK
Canada

In presenting this thesis in partial fulfillment of the requirements for a Postgraduate degree from the University of Saskatchewan, I agree that the Libraries of this University may make it available for inspection. I further agree that permission for copying of this thesis in any manner, in whole or in part, for scholarly purposes may be granted by the Head of the Department or the Dean of the College in which my thesis work was done. It is understood that any copying or publication or use of this thesis or parts thereof for financial gain shall not be allowed without my written permission. It is also understood that due recognition shall be given to me and to the University of Saskatchewan in any scholarly use which may be made of any material in my thesis.

Requests for permission to copy or make other use of material in this thesis in whole or in part should be addressed to:

Head of the Department of Physics and Engineering Physics
116 Science Place
University of Saskatchewan
Saskatoon, Saskatchewan
Canada
S7N 5E2

Abstract

A novel photon flux monitor has been designed and tested for use at the Duke University High Intensity Gamma Source, where the photon beam produced is essentially mono-energetic but it is not tagged. Direct counting of the number of photons using a high-efficiency detector is not possible because of the high photon fluxes expected. Therefore, a direct counting detector with a low, accurately known efficiency was required.

The photon flux monitor based on a five scintillator paddle system detects recoil electrons and positrons from photoelectric, Compton and pair-production processes. It has been designed to be insensitive to gain and detector threshold changes and to be usable for photon energies above 5 MeV. It has been calibrated using direct counting with a NaI detector and its efficiency has been shown to be well predicted by a GEANT4 simulation.

Results of measurements, calibration and calculations required to characterize the 5-paddle photon flux monitor are presented. The photon flux monitor has met its design specifications of being able to determine the number of photons incident on it during the live time of a measurement to within a systematic error of 2%.

A paper based on the work for this thesis has been published in the Nuclear Instruments and Methods in Physics Research Journal. [Pyw09]

Acknowledgements

I want to take the opportunity to forward my words of appreciation to my supervisor, Professor Rob Pywell, for his continuous and invaluable guidance and encouragement. This thesis could not have been written without his constant help and support.

A big thank you to my colleague Ward Wurtz for providing invaluable assistance and an example to follow. Brian Bewer and Daron Chabot will always be remembered for making me feel welcomed in the Subatomic Physics group. I thank also our summer student, Robin Wilson, and the team from the Physics machine shop, Pery Balon, Blair Chomyshen and Ted Toporowski.

My gratitude is also expressed to members of my advisory committee: Professor Rainer Dick, Professor Ru Igarashi and Professor Gap Soo Chang for their comments and suggestions and for constantly helping me through the entire process of graduation.

Nevertheless, all the people from the Physics Department at the University of Saskatchewan earned my deepest respect.

The financial assistance of the Natural Science and Engineering Research Council (NSERC) of Canada is gratefully acknowledged. I would also like to thank all the members of the TUNL group at Duke University for their assistance in making the characterization measurements for the flux monitor.

I feel it is the time to express heartily regards to two special people, Mireille Jiga and Coriolan Rus, my physics teachers from elementary and high school.

I want to express my entire gratitude to my mother, Teodora Mavrichi, for everything she has given me.

Finally, and importantly, I am thankful to my wife, Manuela Ioana Haias, for her full support and encouragement. She constantly put in me the circumstances that have allowed me to succeed.

To my father, Dr. Dumitru Mavrichi (1927-1990)

Contents

List of Figures

List of Tables

List of Abbreviations

ADC	Analog to Digital Converter
DFELL	Duke Free Electron Laser Laboratory
FEL	Free Electron Laser
GEANT	Particle Physics Simulation Package
HIGS	High Intensity Gamma Source
IR	Infrared Radiation
LUCID	Data Analysis Software
OK-4	Optical Klystron (linearly polarized gamma-rays)
OK-5	Optical Klystron (circularly polarized gamma-rays)
PMT	Photomultiplier Tube
PSD	Pulse Shape Discrimination
TUNL	Triangle Universities Nuclear Laboratory
VME	Versa-Module Eurobus
VUV	Vacuum Ultraviolet Light

Chapter 1

Introduction and Motivation

A measurement of high interest for experimental nuclear physicists is the probability that a particular nuclear reaction will take place. The Subatomic Physics group from the University of Saskatchewan is focused on photodisintegration experiments which involve firing high energy photons at material and observing what comes out (e.g. neutrons, protons, etc.) and how it comes out (e.g. direction, energy). In particular we measure the probability of reactions in which neutrons are emitted and detected. These are known as photoneutron reactions. These experiments are carried out at the High Intensity Gamma Source (HIGS), at Duke University, N.C.

The quantity that essentially gives the measure of the probability for a nuclear reaction to take place is the cross section. Subatomic physics has now reached a point where precision cross section measurements have become necessary to expand our understanding of nuclear forces and the properties of fundamental particles. The measurement of this probability is the main goal of our research group.

An approximate mathematical expression linking together the number of neutrons detected from a reaction, N_n, with the reaction's probability, P, and the number of incident photons, N_γ, is given by:

$$N_n = \varepsilon_n N_\gamma P \tag{1.1}$$

where ε_n is the efficiency of the detector.

The reaction probability is proportional to both the number density of nuclei in the target, n, and the thickness of the target, t, i.e. $P = nt\sigma$. Therefore, the cross section σ is related to the probability of a reaction occurring for a particular nucleus, with the target geometrical factors removed.

Therefore, in order to determine the cross-section, there is not only a need to count the number of neutrons emitted, but the number of incident photons and the efficiency of the neutron detectors need to be known as accurately as possible. The neutron detector's efficiency is the focus of another colleague's work. The measurement of the number of incident photons is a high priority for our research, and has become my Thesis project. The rate of photons is commonly called the "flux" and hence our device for counting the number of photons is called a photon flux monitor.

There were certain features taken into account in the design of the photon flux monitor. Within the goals, the flux monitor has to be stable over a long period of time, it has to be insensitive to gain/threshold shifts and the output of the monitor has to be counted with a simple computer readable counter known as a scaler. That output should be directly proportional to the number of photons incident on the monitor.

The following chapters document the design, construction, and testing of the photon flux monitor. A brief discussion of the theoretical aspects of photon interactions with matter will be followed by a review of photon detection and detectors. A short description of the research facility where the photon flux monitor was tested and commissioned will also be covered. The chapter will describe the production of high energy gamma rays at HIGS, as well as the neutron detector used to measure the photoneutron reaction cross section. That will be followed by a description of the development and construction of the photon flux monitor. A description of calibration and performance tests, along with results and conclusions will be given in the last two chapters.

Chapter 2

Detection of Photons

2.1 The Interactions of Photons

Before describing the design, construction and performance tests of the 5-paddle photon flux monitor, a review of the physical principles involved with the detection of photons is useful. The photon's behavior in matter is dramatically different from that of charged particles. The photon's lack of an electric charge makes impossible the many interactions with atomic electrons which characterize the charged particles. The name γ-rays was given by Rutherford to describe the electrically neutral radiation emitted by naturally occurring radioactive materials. Usage has given γ-rays the meaning of a photon associated with a nuclear or a particle process. [Wil91]

When γ-rays pass through matter, the probability for absorption is proportional to the thickness of the layer of material. Intensity decreases exponentially with this thickness:

$$I(d) = I_0 e^{-\mu d} \qquad 2.1$$

where, $\mu = n \times \sigma$ is the absorption coefficient, measured in cm^{-1}, n = the number of atoms per cm^3 in the material, σ = the absorption cross section in cm^2, I_0 = the incident beam intensity, and d is the thickness of material, expressed in cm.

Photons interact with materials mainly through three processes: the photoelectric effect, Compton scattering and pair production. Other processes, like nuclear dissociation reactions, are possible but these are of very much lower probability for the gamma-ray energies that are expected at HIGS. Each of these processes have separate mechanisms, and occur at different rates depending on energy, and result in different amounts of energy being transferred to the

electrons in the medium. A brief theory behind the main photon interactions is given in order to generate a clear picture of how photons can be detected.

2.1.1 The Photoelectric Effect

The photoelectric effect involves the absorption of a photon by an atomic electron followed by the ejection of the electron from the atom:

$$\gamma + \text{atom} \rightarrow \text{atom}^{+} + \text{e}$$

The photoelectric cross section is given by:

$$\sigma_{photo} = 4\alpha^2 \sqrt{2} Z^5 \sigma_0 \left(\frac{m_e c^2}{h\nu} \right)^{\frac{7}{2}} \text{ (per atom), [Leo94]} \qquad 2.2$$

where: $\alpha = \frac{1}{137}$ is the fine structure constant, $m_e = 0.511$ MeV/c^2 is the electron mass, $h\nu$ is the incident photon energy, Z is the atomic number of the medium, and c is the speed of light.

There are distinctive "edges" in the cross section where the binding energy of an atomic electron is near the photon energy. At these photon energies, the cross section presents a sudden change when the photon energy becomes large enough to eject electrons from a particular shell. Therefore the above equation is only valid for photon energies above the K-shell. The equation also assumes that the electron energies are non-relativistic (i.e. $h\nu << m_e c^2$).

A photon that interacts with matter through the photoelectric effect is absorbed, in which case there will be a total transfer of the photon's energy to the electron. This property is beneficial for the purpose of detection and measurement. However, it should be noted that the cross section for this process drops off quickly with the increasing photon energy and is especially low for a medium with a small atomic number Z.

2.1.2 Compton Scattering

Compton scattering is the process in which photons become scattered by free electrons:

$$\gamma + \text{e} \rightarrow \gamma + \text{e}$$

The electrons in matter are bound but if the binding energy is small compared to the photon energy, they can be considered quasi-free. This consideration gives the possibility to express the kinematics of the process using energy and momentum conservation.

The differential cross section for Compton scattering from a single free electron is given by the Klein-Nishina formula [Leo94],

$$\frac{d\sigma}{d\Omega} = \frac{r_e^2}{2} \frac{1}{[1+\kappa(1-\cos\theta)]^2} \left[1+\cos^2\theta + \frac{\kappa^2(1-\cos\theta)^2}{1+\kappa(1-\cos\theta)}\right], \qquad 2.3$$

where: r_e is the classical electron radius, κ is the incident photon energy over the electron rest energy, $\kappa = h\nu / m_e c^2$, θ is scattering angle of the photon, and $d\Omega$ is the solid angle.

Integrating over all solid angles and multiplying by the atomic number of the medium, Z, the equation for the total cross section for Compton scattering becomes:

$$\sigma_{Compton} = 2\pi Z r_e^2 \left\{\frac{1+\kappa}{\kappa^2}\left(\frac{2(1+\kappa)}{1+2\kappa} - \frac{1}{\kappa}\ln(1+2\kappa)\right) + \frac{1}{2\kappa}\ln(1+2\kappa) - \frac{1+3\kappa}{(1+2\kappa)^2}\right\} \qquad 2.4$$

The formula shows that the cross section has a linear Z dependence and drops with increasing photon energy.

The energy deposited in a medium by a photon through Compton scattering is dependent on the scattering angle, θ, and the thickness of the medium. The energy transferred to an electron divided by the electron rest energy, E_{e^-}, in a single interaction, can be described in terms of θ as:

$$E_{e^-} = \kappa\left(1 - \frac{1}{1+\kappa(1-\cos\theta)}\right) \qquad 2.5$$

After the initial interaction there is still a probability for the photon to interact again and deposit more energy.

Compton scattering is considered to be the principal absorption mechanism for gamma rays in the intermediate energy range 100 keV to 10 MeV and the process is not strongly dependent of the atomic number of the absorbing material.

From the Klein-Nishina formula two useful quantities can be calculated: the Compton scattered and Compton absorption cross sections. The Compton scattered cross section, σ^{s}, is defined as the average fraction of the total energy contained in the scattered photon, while the absorption cross section, σ^{a}, is the average energy transferred to the recoil electron. Another useful formula is for the maximum recoil energy of the electron (Compton edge):

$$E_{\max} = h\nu\left(\frac{2\kappa}{1+2\kappa}\right) \qquad 2.6$$

Related to Compton scattering are the classical processes of Thomson and Rayleigh scattering. Thomson scattering is the scattering of photons by a free electrons in the classical limit. At low energies with respect to the electron mass, the Klein-Nishina formula reduces to the Thomson cross-section:

$$\sigma = \frac{8\pi}{3} r_e^2 \qquad 2.7$$

where $r_e = 2.818 \times 10^{-15}$ m. is the classical electron radius.

Rayleigh scattering is defined as the scattering of photons by atoms as a whole. In this case all the electrons in the atom are considered to participate in a coherent manner (coherent scattering). In both the Thomson and Raleigh scattering processes there is no energy transferred to the medium. The atoms remain neither excited nor ionized and only the direction of the photon is changed. For relatively high energies, both Thomson and Rayleigh scattering are very small and therefore their effects can be considered negligible.

2.1.3 Pair Production

Pair production is simplistic defined as the process by which photons in matter transform into electron-positron pairs:

$$\gamma \rightarrow e^{+} + e$$

The condition for energy conservation is that this process can only occur for photons with energies greater than $2m_e c^2$. Furthermore, the conservation of momentum requires the presence of a nucleus.

The cross sections depend on the electric field felt by the photon as it nears an atom. Atomic electrons affect this field by screening the incident photon from the Coulomb field of the nucleus.

The screening parameter, ξ, is defined as:

$$\xi = \frac{100 m_e c^2 h\nu}{E_+ E_- Z^{\frac{1}{3}}} \qquad \text{[Leo94]} \qquad 2.8$$

where E_+ is the total energy of the outgoing positron, E_- is the total energy of the outgoing electron, and $h\nu$ is the initial energy of the photon.
A complete screening is given when $\xi \cong 0$ and no screening is indicated by $\xi >> 1$.

When an electron-positron pair is created a wide range of energy can be deposited in the medium. The amount $2m_e c^2$ is needed to create the pair while the remainder, $h\nu - 2m_e c^2$, goes into their kinetic energy. The pair can afterwards lose energy through ionization of the medium, by annihilation, or by being converted to a photon through the bremsstrahlung interaction with the Coulomb field of a nucleus.

2.1.4 The Total Absorption Coefficient and Photon Attenuation

The total probability for a photon interaction in matter needs to be the sum of the individual cross sections outlined above. Per atom, this yields:

$$\sigma = \sigma_{photo} + Z\sigma_{Compton} + \sigma_{pair}, \qquad 2.9$$

where the Compton cross-section is multiplied by Z to take into account the Z electrons per atom.

Some plots of absorption coefficients versus gamma energy are shown in Figures 2.1 and 2.2 with a comparison between the three different effects.

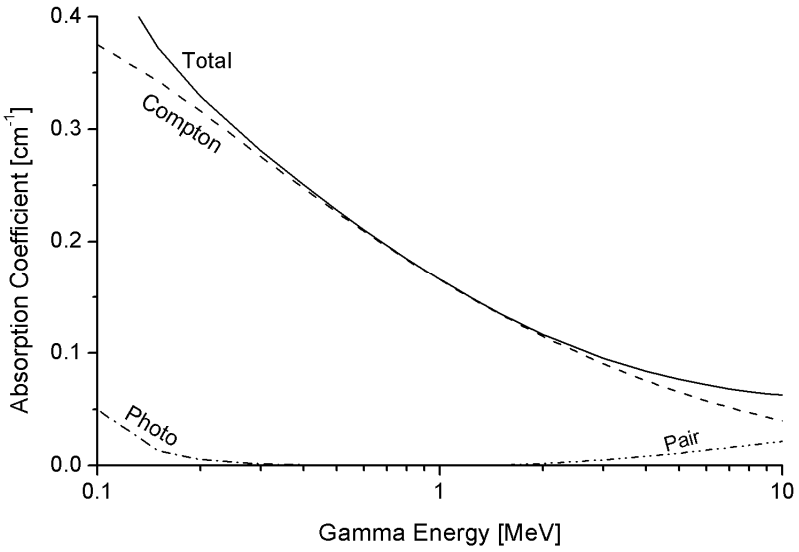

Figure 2.1 The total absorption coefficient of aluminum for gamma rays, plotted versus gamma energy, and the contributions by the three effects. Over most of the energy region shown, the Compton effect dominates. [Diagram courtesy of H. Paul, source Wikipedia]

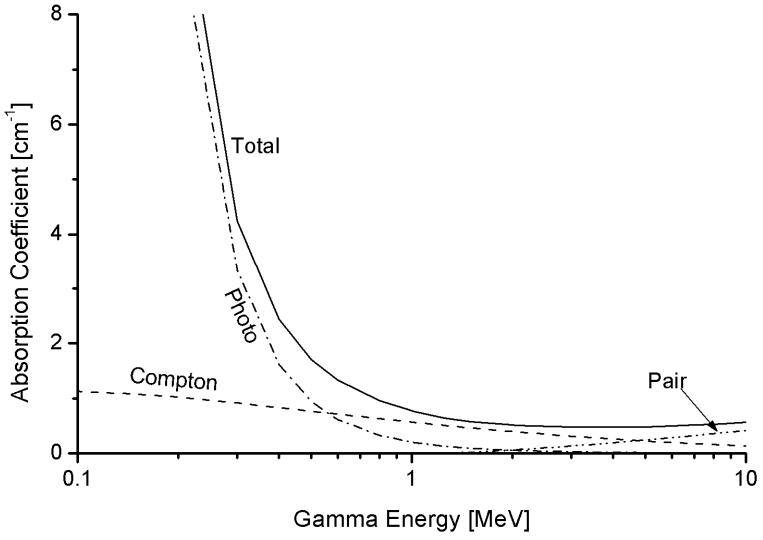

Figure 2.2 The total absorption coefficient of lead for gamma rays, plotted versus gamma energy, and the contributions by the three effects. Here, the photo effect dominates at low energy. Above 5 MeV, pair production starts to dominate. [Diagram courtesy of H. Paul, source Wikipedia]

When multiplying σ by the density of atoms, N, we obtain the total absorption coefficient:

$$\mu = N\sigma = \sigma\left(\frac{N_a \rho}{A}\right) \qquad 2.10$$

with: N_a = Avogadro' number, ρ = density of the material, A = molecular weight.

The total absorption coefficient does not change with the physical state of a given absorber for a given γ-ray energy. For compounds and mixtures, the total absorption coefficient is calculated using Bragg's rule:

$$\frac{\mu}{\rho} = w_1 \frac{\mu_1}{\rho_1} + w_2 \frac{\mu_2}{\rho_2} + \ldots, \qquad 2.11$$

where w_i = the weight fraction of each element in the compound or mixture.

2.1.5 Buildup

When monoenergetic γ-rays are collimated into a narrow beam and strike a detector after passing through an absorber of variable thickness (t), the result should be a simple attenuation of the γ-rays. γ-ray photons are removed from the beam either by absorption or by scattering away from the detector direction and can be characterized by a fixed probability of occurrence per unit length in the absorber. The Figure 2.3 depicts a γ-ray attenuation experiment that can be characterized as a "narrow beam" or "good geometry" measurement. The essential characteristic in this case is that only γ-rays from the source that escaped interactions in the absorber can be counted by the detector.

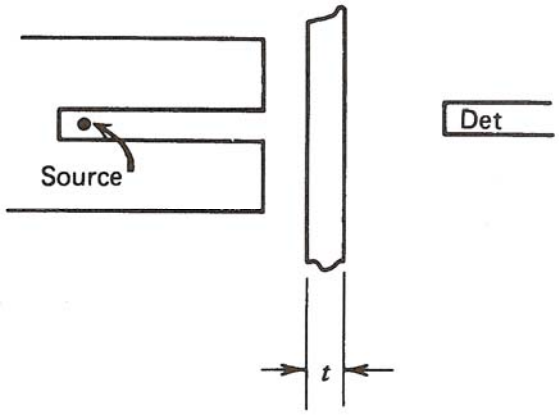

Figure 2.3 A gamma-ray attenuation experiment measured under "good geometry" conditions ([Kno00])

In “real life” measurements are mostly carried out under different circumstances in which the severe collimation of the γ-ray is absent (Figure 2.4).

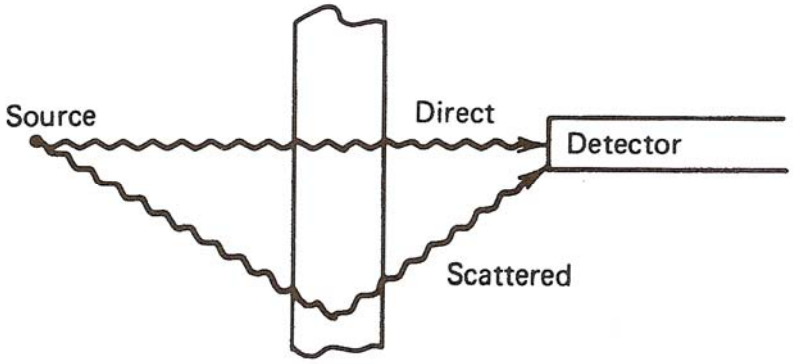

Figure 2.4 Real conditions of measurements for an attenuation experiment ([Kno00])

In this case, more close to the practical reality, the detector can respond either to γ-rays directly from the source, to γ-rays that strike the detector after suffering scattering in the absorber, or to other types of secondary photon radiation. Therefore, conditions that lead to the simple exponential attenuation are violated in what is defined as a “broad beam” or “bad geometry” measurement. This situation with the additional contribution of the secondary γ-rays is described by

$$\frac{I}{I_0} = B(t, E_\gamma)e^{-\mu t}, \qquad 2.12$$

where I is the number of transmitted photons, I_0 is the number without an absorber, μ is the linear attenuation coefficient which is the sum of probabilities per unit path length t, and $B(t, E_\gamma)$ is called the buildup factor. The buildup factor is introduced as a simplistic multiplicative correction due to the major variation of the γ-ray counting rate with absorber’s thickness. The factor depends on the type of detector used and on the geometry of the experiment. For thick slab absorbers the buildup factor tends to be about equal to the thickness of the absorber (measured in units of mean free path of the incident γ-ray) [Kno00]. In a practical design, such as the flux monitor described in this thesis, the buildup factor is not directly calculated, but the effect is accounted for by using a Monte-Carlo calculation.

2.2 Scintillation and Scintillator Detectors

In this research toward detecting and counting photons, the workhorse is the scintillator counter. A scintillation counter is composed of a scintillation medium, a light detector, and a light guide to transfer the light from one to the other (Figure 2.5). A brief description of each of the components of a scintillation detector follows.

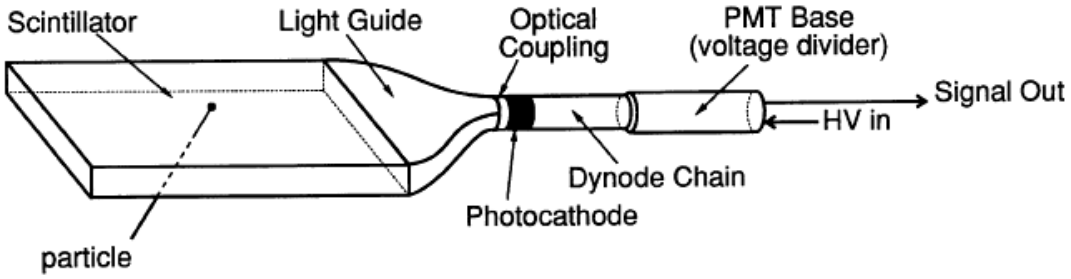

Figure 2.5 A typical scintillator system consisting of a scintillation medium, light guide, and light detector [Arm00]

2.2.1 Scintillation Process

Scintillation is the process by which certain materials emit small flashes of light (i.e. a scintillation) when struck by a subatomic particle or radiation. When designing a beam monitor, scintillation caused by the physical processes involved and the efficiency with which these processes convert incident radiation to light need to be known. The scintillations can be converted, after amplification, into electrical pulses which can be analyzed and counted electronically.

Scintillator materials can be inorganic and organic, and both types have fundamentally different mechanisms responsible for their light emitting characteristic. Usually, the inorganic scintillators are crystals with added impurities and include NaI(Tl), CsI(Tl), LiI(Eu) and BGO. Organic scintillators are mostly polymerized solids and include anthracene and naphtalene.

The mechanism for inorganic scintillation starts when the incident ionizing radiation excites an electron from the valence band to the conduction band. With the jump back of the electron into the valence band an energy equivalent to the band gap, usually 5 to 10 eV, is released as a

photon. The incident radiation can promote a valence electron to another energy level just below the conduction band, which is called the exciton band. The electron in this state is still electrostatically bound to the hole that it left in the valence band and this electron-hole pair (an exciton) can migrate throughout the crystal lattice until it reaches an impurity. Because the impurity has energy levels different from those in the crystal lattice, it can be ionized by the exciton. A subsequent electron arriving at the impurity can be trapped by the ion causing the emission of de-excitation radiation.

The scintillation mechanism for organic scintillators is a multistage fluorescent process. A primary fluorescence agent is responsible for absorbing energy from ionizing radiation by promoting electrons to higher energy levels. It then releases this energy as the electrons return to their ground states. Fluors are other fluorescent materials that need to be present in this mechanism. The fluors absorb the energy emitted by the primary fluorescent agent and emit it as photons with a wavelength that can exit the scintillator. The transfer of energy between the primary fluorescent agent and the fluor is based on a Foerster dipole-dipole interaction. [Gro00]

A schematic diagram of the scintillation mechanism is provided in Figure 2.6.

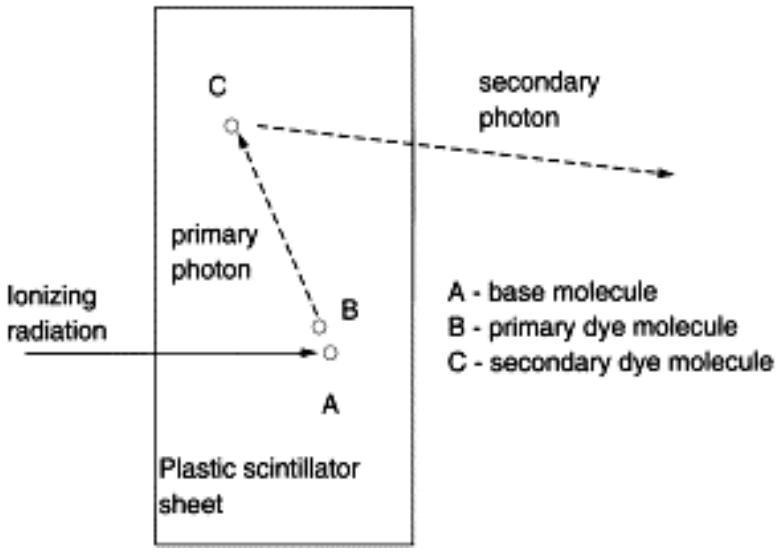

Figure 2.6 Scintillation mechanism ([Kir00])

2.2.2 Scintillator Detectors

Either type of scintillator could be used as the scintillator material but an organic scintillator called BC 400 (plastic scintillator) was chosen for this particular project. Inorganic crystals would have provided the highest photon interaction cross section because of their high atomic number. However, they can be difficult to work with because many of them are hygroscopic and require a protective enclosure to prevent contact with the moisture in the air. Organic scintillators are not hygroscopic and can be dissolved into plastic making them very easy to work with. BC-400 scintillator was readily available in thin (~2 mm thick) sheets which was ideal for our application. Because of our choice, a brief description of plastic scintillators will be provided.

In particle physics measurements, plastic scintillators (solutions of organic scintillators but in a solid plastic solvent) are probably the most widely used of the organic detectors today. Plastics offer an extremely fast light signal with a decay constant of about 2-3 ns and a high light output efficiency. Because of the fast decay, the finite rise time cannot be ignored. A correct mathematical description of the light output as a function of time, $N(t)$, is the convolution of a Gaussian with an exponential:

$$N(t) = N_0 f(\sigma, t) \exp(\frac{-t}{\tau}), \qquad 2.13$$

where: $N(t)$ = the number of photons emitted at time t, N_0 = the total number of photons emitted, τ = the decay constant, and $f(\sigma, t)$ is a Gaussian with a standard deviation σ.

The plastics' flexibility is one of their most important qualities. They can be easily cut or shaped to desired forms, but because of their softness (softening begins at about 75 ^{o}C) certain techniques (e.g. diamond machining) need to be applied, in order to obtain high-quality surfaces. Extra-fine polishing (the method used for this project) is a very good and convenient alternative for the same high-quality surfaces. Different types of plastics offer differences in light transmission, speed, etc.

During measurements, plastic scintillators are exposed to sustained high levels of radiation and so, particular attention has been paid to the degradation in the scintillator output due to radiation damage. [Vas96] This process is complicated, with many variables including the dose rate, the

presence or absence of oxygen, and the nature of the radiation. Some recovery or annealing of the damage can be possible over periods of time that differ from hours to days following an exposure. However, significant degradation in light yield is observed for cumulative gamma-ray exposures in the range of 10^3 or 10^4 Gy. [Kno00]

In general, the scintillator signal is capable of providing a variety of information. Some of the most important scintillator features are:

- *Sensitivity to energy*. Above a certain minimum energy, most scintillators behave in an almost linear fashion with respect to the energy deposited. In this ideal case the light output is directly proportional to the exciting energy. Since the photomultiplier tube (PMT) is also a linear device (if used properly), the amplitude of the final electrical signal will also be proportional (for many applications it can be considered a good approximation) to this energy:

  $$L \propto \Delta E , \qquad 2.14$$

  where: L = the fluorescent light emitted, and ΔE = the energy deposited by the ionizing particle.

  In reality, the response of scintillators is a complex function that has to take into account the type of particle and its specific ionization.

- *Fast time response*. Scintillator detectors' response and recovery times are short relative to other types of detectors. This feature allows us to measure with good precision the time between two events. The fast recovery time means that the dead time (the time during which a second event cannot be counted) is reduced, and so scintillator detectors can accept higher count rates.

- *Pulse Shape Discrimination (PSD)*. Some scintillators are capable of PSD, which means they are capable of distinguishing between different types of incident particles by the shape of the emitted light pulse. This, however, is not an important consideration for our application. Our chosen scintillator, BC-400, does not have good PSD qualities.

- *Light output*. It is an extremely important quantity, as it determines the efficiency for converting ionization energy into photons and therefore will affect the energy resolution of the scintillator. In general the light output is different for different types of particles at the same energy and for a given particle it does not always vary linearly with energy. When considering the efficiency of a scintillation detector, the efficiency of the PMT must also be taken into account, since they are inseparably coupled.

  For our application we are primarily interested in detecting recoil electrons and positrons. The light output of the scintillator for these particles is, to a very good approximation, directly proportional to the energy deposited in the scintillator. For other particles the response is non-linear [Pyw06]. Although it is a small effect for our application, we have included this non-linearity in the Monte-Carlo simulation used to understand the response of the photon flux monitor.

- *Absolute scintillation efficiency*. Absolute scintillation efficiency, η, refers to the ratio of visible light energy emitted by a scintillator to the energy deposited in the scintillator by incident radiation. This parameter can be used, in conjunction with energy deposition predictions from a computer simulation, to model the intensity of light given off by a scintillator that is placed in a gamma-ray beam.

  A complex method for theoretically calculating the absolute scintillation efficiency of a given material is provided by Birks. [Bir64] For the design purposes encountered in this project it is sufficient to use efficiency values given by the manufacturer. It is customary for a manufacturer to specify the efficiency of a scintillator as a percentage of the absolute efficiency of anthracene which has an absolute efficiency of 0.04.

  The BC-400 plastic scintillator used for this project has a relative efficiency of 65%, giving it an absolute scintillation efficiency of 0.03. Some characteristics of the BC-400 are presented in Table 4.1 in Chapter 4. In practice it is not necessary to know the absolute scintillation efficiency since the response of a detector will usually be calibrated using a radiation source of known energy.

- *Dead Time Losses from Pulsed Sources*. If the source of radiation is not continuous but consists of short pulses repeated at a constant frequency, the scenario for the detectors' counting could be:
  1. If the relative value of the detector's dead time, τ, is much smaller than the duration of each pulse, T, the fact that the source is pulsed has little effect;
  2. If τ is less than T but not by a large factor, only a small number of counts may be registered by the detector during a single pulse;
  3. If τ is larger than T but less than the "off" time between pulses, we can have a maximum of only one detector count per source pulse. In this case, the detector will be fully recovered at the start of each pulse. [Kno00]

  We will see that scenario 3 is most appropriate for our application.

2.2.3 Light Guides

It is sometimes inadvisable or even impossible to couple a photomultiplier tube (PMT) directly to one face of a scintillator. Light collection can be achieved by using a transparent solid, known also as a light pipe or light guide, to physically couple the scintillator to the PMT and to act as a guide for the scintillator light.

Light guides are generally optically transparent solids with a relatively high index of refraction to minimize the critical angle for total internal reflection. Their surfaces need to be highly polished and are usually surrounded by a reflective wrapping material to direct back some of the light that escapes at angles less than the critical angle.

In general, the scintillator refractive index determines the fraction of light collected. This is particularly true when the scintillator is long in the direction perpendicular to the light entrance surface. Beside the refractive index, the cross-sectional area of the scintillator perpendicular to the light direction contributes to transmitting the light through the light guide. If this is maintained constant along the light guide (and also at the coupling area to the PMT) and sharp bends are avoided, then the light guide can theoretically transmit all the light that enters. Another important factor is the photocathode area of the PMT which has to be at least as large as the light guide surface area that comes in contact with.

2.2.4 Photomultiplier Tubes

The photomultiplier tube (PMT) accomplishes the conversion of the extremely weak light output of a scintillator pulse into a corresponding electrical signal. PMTs are able to convert light signals that typically consist of no more than a few hundred photons into a usable current pulse without adding a large amount of random noise to the signal. PMTs may be operated in continuous mode, i.e., under a constant illumination, or in pulsed mode as in the case in scintillation counting.

The simplified structure of a typical PMT (together with the scintillator cell) is presented in Figure 2.7:

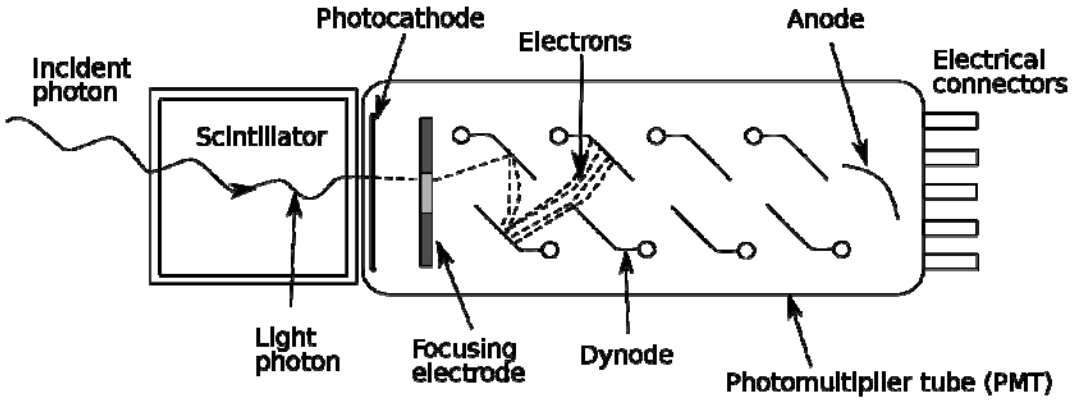

Figure 2.7 Photomultiplier structure [Diagram courtesy of Colin Eberhardt, source Wikipedia])

The tube contains a thin photosensitive layer, the photocathode, and the electron multiplier structure. An outer envelope (usually glass or quartz) serves as a pressure boundary to sustain vacuum conditions inside the tube. The vacuum condition is required so that low-energy electrons can be efficiently accelerated by internal electric fields. The photocathode's purpose is to convert as many of the incident light photons as possible into low-energy electrons. In a typical pulse only a few hundred photo-electrons may be involved and their charge is too small to be measured as a convenient electrical signal. Therefore, a high voltage is applied to the cathode, multiplier structure (dynodes), and anode such that a potential "ladder" is set up along the length of the cathode-dynode-anode system. This potential determines the production of more and more secondary electrons to be emitted from dynodes and thus, an electron cascade

down the dynode string is created. After amplification, a typical scintillation pulse will give rise to 10^7-10^8 electrons, enough to serve as the charge signal for the original scintillation event. This charge is collected at the anode.

The photocatode converts the incident light into a current of electrons through the photoelectric effect. Einstein's formula, $E = h\nu - \phi$, (E = the kinetic energy of emitted electron, ν = the frequency of incident light and ϕ = the work function), shows that a certain minimum frequency is required for the photoelectric mechanism to take effect.

The frequency of the incident light and the structure of the material control the efficiency for photoelectric conversion. The overall spectral response can be expressed by the quantum efficiency, $\eta(\lambda)$,

$$\eta(\lambda) = \frac{\text{number of photoelectrons released}}{\text{number of incident photons on cathode } (\lambda)}\ , \qquad 2.15$$

where λ is the wavelength of the incident light. The quantum efficiency would be 100% for an ideal photocathode. Real photocathodes show a maximum quantum efficiency of 20-30%.

An equivalent quantity is the radiant cathode sensitivity:

$$S(\lambda) = \frac{I_k}{P(\lambda)}\ , \qquad 2.16$$

where I_k is the photoelectric current from the cathode, and $P(\lambda)$ is the incident radiant power. The radiant cathode sensitivity, $S(\lambda)$, is usually given in units of ampere/watt and its relationship to the quantum efficiency is:

$$S(\lambda) = \lambda\eta(\lambda)\frac{e}{hc} \qquad 2.17$$

The spectral response of a photo material is in general such that only a certain band of wavelength is efficiently converted. Therefore, a very important consideration when choosing a PMT should be its radiant sensitivity to the wavelength of the incident light.

Regarding the design of the dynode system, the following requirements must be met:

- collection must be as efficient as possible, i.e. as many emitted electrons as possible must reach the dynode system regardless of their point of origin on the cathode;
- the necessary time for an emitted electron to travel from the cathode to the first dynode must be as independent as possible of the point of emission.

The gain of each dynode is known as the secondary emission factor, δ. The mechanism of secondary electron emission is very similar to that described for photoelectric emission except that the photon is now replaced by an electron.

A good dynode material needs to meet the following requirements:

- to have a high secondary emission factor, δ, i.e., the average number of secondary electrons emitted per primary electron;
- to present a good stability of secondary emission effect under high currents;
- to produce a low thermionic emission, i.e., low noise.

PMTs usually contain 10 to 14 stages (in different geometries), obtaining a total overall gain of up to 10^7. The gain (or the overall amplification factor) of a PMT depends on the number of dynodes and the secondary emission factor, which is a function of the energy of the primary electron. Therefore we can write:

$$\delta = KV_d \ , \tag{2.18}$$

where V_d is the potential difference between dynodes, and K is a proportionality constant.

Considering that the applied voltage is equally divided among dynodes, the overall gain of the PMT is:

$$G = \delta^n = (KV_d)^n \tag{2.19}$$

with n = the number of stages.

Conventional dynode materials are characterized by a typical value of $\delta = 5$, with K being near unity for well-designed tubes. A 10 stage PMT will therefore result in an overall gain of 5^{10}, or about 10^7.

Another important relation is the gain variation with respect to supply voltage:

$$\frac{dG}{G} = n\frac{dV_d}{V_d} = n\frac{dV_b}{V_b} \qquad 2.20$$

with V_b = the minimum supply voltage (for a fixed gain). This shows us that, for example, for $n = 10$, a 10% variation in gain implies a 1% change in V_b. Thus, to maintain a gain stability of 1%, the voltage supply must be regulated to within 0.1%. This example only reflects the fact that the gain stability of a PMT is one of its most important characteristics.

The gain stability can be influenced by different factors. In general, variations in gain (also known as fatigue effects) are most likely due to unwanted changes somewhere in the dynode system. Two types of changes can be distinguished:

- drift, which is a variation in time under a constant level of illumination;
- shift, a sudden change in the gain after the current has changed (sometimes known as count-rate shift).

The gain changes may not be fully reversible, and hysteresis effects have been observed experimentally. [Bew05, Yam77]

Chapter 3

The High Intensity Gamma Source and the Blowfish Neutron Detector

3.1 The High Intensity Gamma Source

The University of Saskatchewan's Subatomic Physics group is involved with photodisintegration experiments using the High Intensity Gamma Source (HIGS). This is the newest accelerator facility operated by the Triangle Universities Nuclear Laboratories (TUNL) at the Duke Free Electron Laser Laboratory (DFELL), located on the campus of Duke University.

A diagram showing the gamma-ray production is presented in Figure 3.1. The operating principle at HIGS is the Compton backscattering of the free-electron laser (FEL) photons in the storage ring. A 280 MeV linear accelerator is used to inject electron bunches into the storage ring where they can be accelerated up to 1.2 GeV. In FEL-mode, a single electron bunch travels through a set of wigglers (or undulators), a region of rapidly alternating magnetic fields, emitting synchrotron light which is reflected back and forth between the mirrors. The emitted light is coherent with a polarization defined by the wiggler magnetic field. The resulting laser light has a wavelength that is continuously tunable wavelength, from IR to VUV, by changing the electron beam energy and the magnetic field strength of the wiggler.

When gamma-rays are needed, a second electron bunch is injected into the ring exactly halfway around the orbit relative to the initial bunch. The second bunch enters the straight section of the ring and collides head on with the FEL photons generated by the first bunch. Some fraction of

the FEL photons will scatter and will get a boost in their energy. The two electrons bunches contained in the storage ring act as a lasing bunch and a scattering bunch. This scattering process in which the FEL photons and the electrons share the same beam pipe is known as intra-cavity scattering. The resulting gamma-rays are no longer reflected by the mirror at the right end of the optical cavity and are collimated for use in the experimental vault. The backscattered gamma rays maintain the polarization and tight energy spread of the FEL photons providing a very clean, virtually monoenergetic, polarized (with polarization greater than 90%) gamma-ray beam. [Reg03, Saw05]

The gamma-ray beam energy is tunable by adjusting the electron energy and magnetic field strength in the wigglers. [Wel03] The total beam flux before collimation is greater than 100 million gamma/s. Using collimation, the energy spread of the gamma-ray beam is selectable down to about 1%. The current gamma-ray beam capabilities include reliable delivery of a nearly mono-energetic linearly or circularly polarized gamma-ray beam to target in the energy range from 2 to 60 MeV. The flux of gamma rays can be increased by increasing the current in the target bunch and/or by operating eight electron bunches.

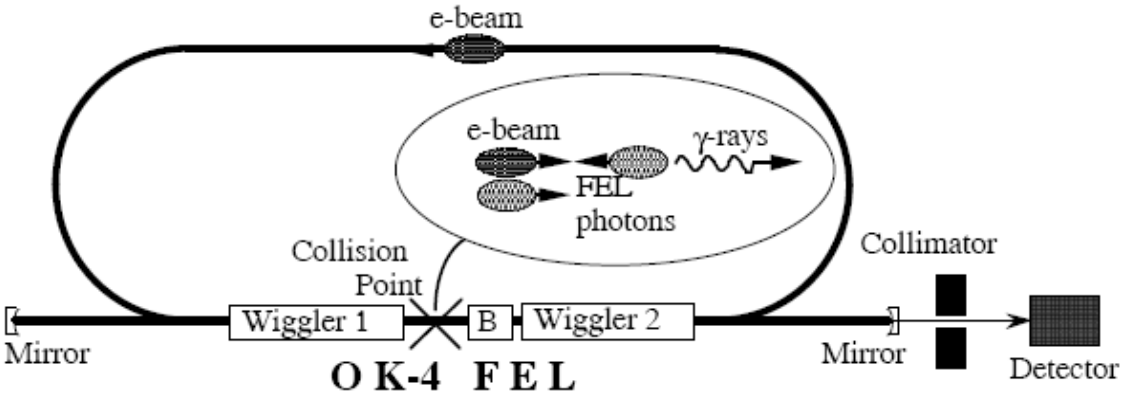

Figure 3.1 Schematic diagram of the HIGS - the DFELL-TUNL - ray facility ([Wel03])

The system is self-aligning with respect to producing gamma rays, since the electron beam and the photon beam need to be collinear for lasing to occur. This result in an intensity gain of about 1000 compared to that obtained when using an external laser, since the lased light does not need to be extracted from the cavity. The excellent vacuum conditions mean that bremsstrahlung

photons, which have a continuous energy spectrum, and result from electrons hitting residual gas in the vacuum pipe, are nearly absent. The only source of beam related background is that generated by collimation, which is reduced by post-collimation shielding.

Because of the nature of gamma-ray production at HIGS, the beam has a definite time structure which can be exploited. A burst of gamma-rays is produced each time a collision happens in the optical cavity. Because the frequency is 5.58 MHz per bunch, a collision takes place every 180 ns in the two-bunch mode of operating. This structure allows time-of-flight techniques to be employed in order to distinguish beam-related events from room background.

The HIGS facility was recently upgraded (Figure 3.2) with the installation of a Booster-Injector, a new RF cavity and a new optical klystron (OK-5). [Bla07]. The Booster can accelerate electrons to any energy between 0.23 and 1.2 GeV before injecting into the storage ring. This allows electrons to be transferred to the storage ring on a relatively continuous basis to replenish lost electrons. The new optical klystron (OK-5) accomplishes the delivery of gamma-rays in different polarization vectors, linear (horizontal, vertical), and circular (forward, backward), with respect to the direction of the photons.

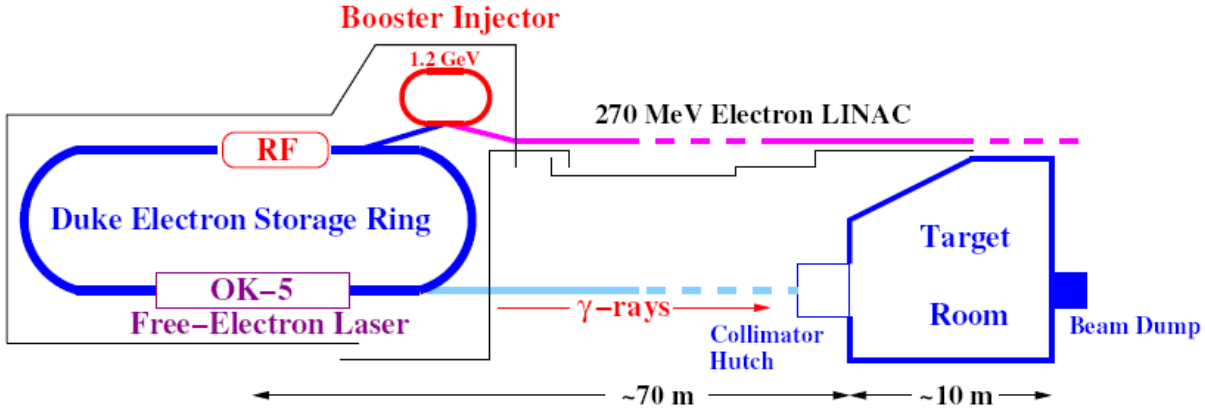

Figure 3.2 Layout of the HIGS facility with the full-energy booster injector and the new helical undulator (OK-5) [Wel03]

Taking into account all the above, the HIGS facility is properly suited for experiments where high flux, large photon density, low beam background, high beam polarization and high energy resolutions are a necessity.

3.2 The Blowfish Neutron Detector

The Blowfish array, currently in use at HIGS, is one of the key neutron detector packages available and was built to study the photodisintegration of light nuclei. During a photodisintegration experiment, a target is placed inside Blowfish (Figure 3.3) and gamma rays are fired at the target. The detection is due to 88 BC-505 liquid scintillator cells (neutron detectors) located on the surface of a 16" diameter sphere centered on the target in 8 uniformly spaced arms (11 detectors on each arm uniformly distributed between polar scattering angles). The broad coverage (a quarter of a sphere) of the detector together with its ability to be rotated about the beam axis permits high statistical precision and accurate determination of systematic effects. In order to detect neutrons (using an indirect method), the 88 detectors used in Blowfish are each composed of a cell containing the BC-505 scintillator liquid, a light guide and a photomultiplier tube (PMT). The liquid scintillator in the cell is rich in hydrogen (mixing ratio H:C=1.331:1). When a neutron coming from the target enters the cell, it may collide with a hydrogen nucleus and transfer energy to the proton. The charged proton perturbs nearby scintillating impurities, causing them to release a photon which can be detected by a PMT. [Leo94] Because of Blowfish's spherical nature, it will be possible to extract the angular dependence of the differential cross section as well as the total cross section.

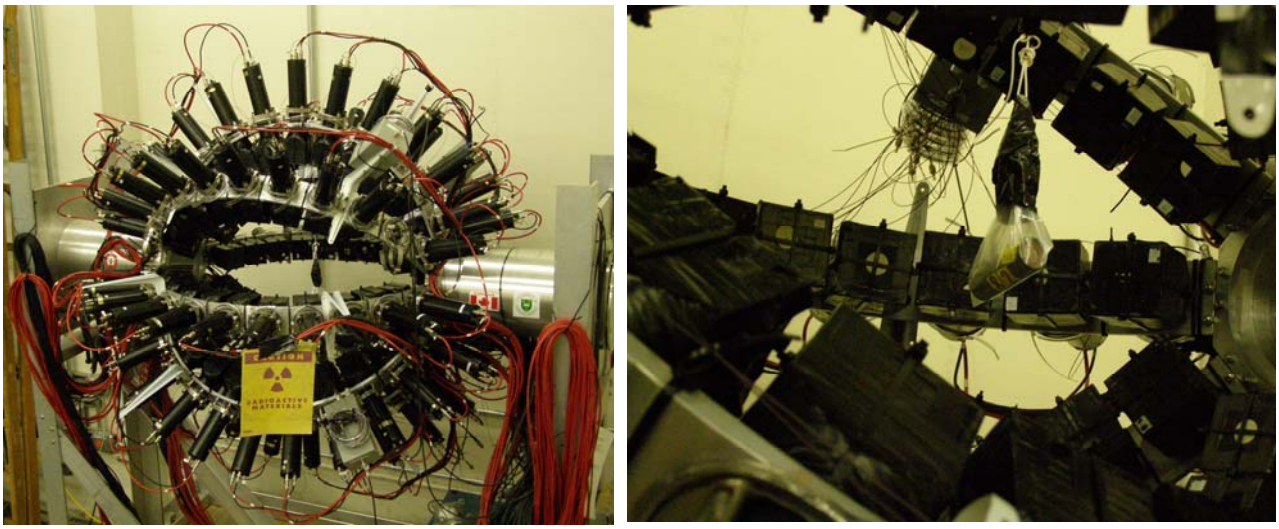

Figure 3.3 The blowfish detector array. Hanging in the middle of the array is a radioactive source (depicted in the right picture)

In the last few years many improvements and upgrades were made to Blowfish to make possible many of the near-threshold and high precision measurements planned for research program. These included: Upgrades to data acquisition electronics hardware and software (LUCID [Mur95]) to allow VME support (Summer Student Project: A. del Frari, and M.Sc. Thesis: D. Chabot [Cha08]) resulting in a 20-fold increase in data rate; A fibre optic light pulser gain monitoring and stabilization system has been designed and installed on all 88 Blowfish cells (M.Sc. Thesis: B. Bewer [Bew05]). This is vital to ensuring that the neutron detection efficiency can be calculated to the required accuracy using a code such as GEANT4 [GEA03]. Significant effort has been put into understanding the response to neutrons of the BC-505 cells and the light output curves for BC-505 have been firmly established [Pyw06].

Chapter 4

Design and Construction

4.1 Flux Monitor Design

4.1.1 Introduction

Considerable advances have been made in understanding the efficiency of nuclear particle detectors. However, for non-tagged photon sources, similar advances have not been made in the accuracy of photon flux measurements.

Many photon counting methods have been used in the past. For bremsstrahlung photon beams ionization chambers have commonly been used, for example the "P2 chamber" [Pru62]. Such devices rely on slow charge integration and so dead-time corrections are necessary since charge is collected while an acquisition system may be busy or stopped. Such dead-time corrections are difficult for modern high-count-rate experiments as they rely on the knowledge of the instantaneous photon flux which may or may not be constant.

Experiments that use photon tagging (for example [Vog93, Ant91, Sob96, Hir06]) count the number of post-bremsstrahlung electrons striking a focal plane detector. This may be related to the number of photons reaching a target by applying a measured "tagging efficiency". The recoil electrons are counted using scalers which may be gated by the live time of the experiment, thus obviating the need for dead-time corrections.

The photon beam from the High Intensity Gamma Source (HIGS) is essentially mono-energetic but is not tagged. Direct counting of the number of photons using a high-efficiency detector

(such as a NaI scintillator or lead-glass Cherenkov counter) is not possible because of the high photon fluxes expected. Therefore a direct counting detector with a low, accurately known efficiency is required.

Design criteria for such a monitor included the following:

- The efficiency of the monitor should be relatively low so that even at high photon fluxes (greater than 1×10^8 photons/s) counting could be accomplished using standard nuclear electronics
- The monitor should be highly selective of interactions caused only by the primary photon beam, and thus insensitive to room background
- The monitor should be weakly dependent on the gain of its components (e.g. drifts in the gain of a photomultiplier tube which in turn affects the energy level at which a discriminator fires)
- The monitor should have a prompt output that can be counted with a scaler that can be gated by the live time of an experiment
- Because the monitor must remain in the photon beam during an experiment it must have low mass to reduce the background radiation produced by it that may interfere with a measurement.

Photon counting detectors, which employ the detection of recoiling photoelectrons, Compton scattered electrons, and pair production electrons and positrons by plastic scintillators, have been used with some success at HIGS [Rey02] and other facilities. However, these devices have not met all the above criteria with sufficient accuracy for high precision cross section measurements. The photon flux monitor described in this thesis is designed to meet the above criteria so that the measurement of photon fluxes, accurate to better than 2%, can be achieved.

4.1.2 Previous Work

The idea and the necessity of a photon flux beam monitor designed for HIGS goes back several years. In 2001 a thin plastic-scintillator paddle attached to a photomultiplier tube was placed so that the beam passes through it. [Ahm07] A fraction of the gamma rays passing through the paddle interact and produce recoil electrons or electron-positron pairs. These particles produce

signals in the paddle proportional to the flux of gamma rays. The response changes slowly with gamma-ray energy so that the paddle is an effective, simple way to monitor the beam intensity. The initial paddle design consisted of a single 1/8" thick NE-102 plastic scintillator optically coupled to a 2" PMT. The signal from the PMT was discriminated and fed into a scaler that was read-out periodically and incorporated into the Blowfish data stream. [Saw05]

However, there is another effect that causes problems with this technique. Energetic electrons and positrons are produced by the gamma-ray beam striking collimators and other structures upstream from the paddle. The number of these electrons depends not only on the beam flux but also upon the particular arrangement of upstream structures and upon the tuning details of the beam itself. These particles may strike the paddle and cause signals that are not directly proportional to the beam flux. This initial paddle configuration lacked any kind of charged particle veto and was sensitive to significant backgrounds from the collimator and other sources. As such, it was really only suitable as a convenient method of monitoring beam intensity during online data taking.

4.1.3 Conceptual Design and Principle

To correct for the problem of charged particles produced upstream from the paddle, the flux monitor was redesigned to reject the counts due to the upstream particles. Therefore, the paddle detector was rebuilt in a 5-paddles configuration. The operating principle behind this device is to restrict oneself to counting only secondary particles generated by an incoming γ-ray. This is accomplished by layering a series of paddle detectors along with a thin piece of material referred to as a radiator.

The photon flux monitor was designed with the aid of a simulation built using the GEANT4 [GEA03] toolkit. Using the simulation it was possible to vary all parameters of the monitor to investigate the sensitivity of its efficiency to changes in such things as discriminator energy levels.

The final conceptual design of the monitor is illustrated in Figure 4.1. Recoil electrons and positrons generated principally in the radiator are identified by a triple coincidence between the

outputs of paddles 2, 3 and 4. An anti-coincidence with a veto paddle (paddle 1) is employed to remove charged particles generated upstream of the radiator.

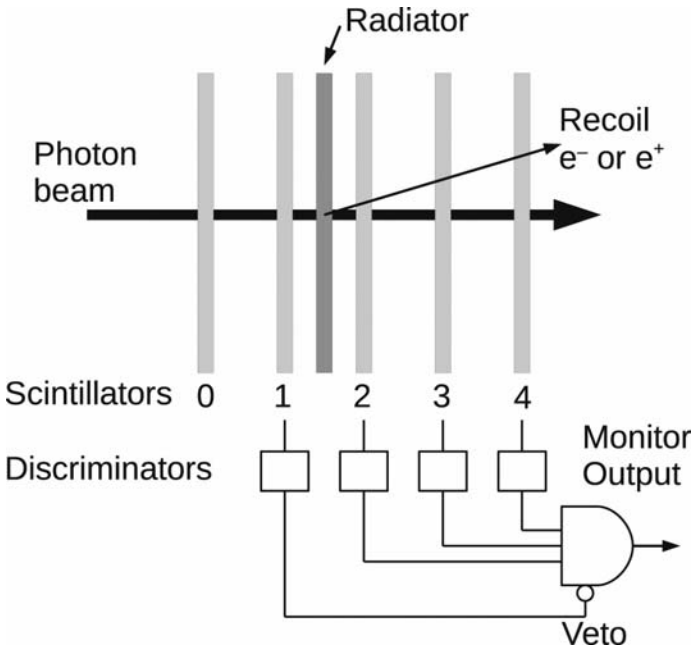

Figure 4.1 Conceptual design of the photon flux monitor

The scintillator paddles are chosen to be thin, about 2 mm thick, to reduce their sensitivity to room background, which, in this environment, includes a fairly large flux of low-energy neutrons. Because the paddles are thin, the energy deposited by electrons and positrons passing through them will be approximately the same regardless of their energy. That is they will behave as approximately "minimum ionizing" particles. Therefore, with a discriminator threshold set well below the minimum ionizing peak, the efficiency of each paddle for detecting such particles will be largely insensitive to gain shifts.

Some electrons and positrons that cause a triple coincidence in paddles 2, 3 and 4 while having no hit in the veto can be generated from places other than in the radiator. In particular, in paddle 2 from places closest to the radiator where enough energy is deposited to be over the discriminator's threshold, and in paddle 1 from places closest to the radiator where insufficient energy is deposited to be over the veto paddle threshold. Therefore the efficiency of the monitor does depend on the gain of paddles 1 and 2 more strongly than for the other paddles. However, the inclusion of a radiator greatly reduces this dependence since the majority of the minimum

ionizing particles will be generated in it. The radiator material needs to be of sufficiently high atomic number so that the Compton, photoelectric and pair production cross sections are significantly higher than in scintillator material, while having low nucleon number so that background-producing nuclear reaction cross sections are not too high. Aluminum was chosen as a reasonable compromise while being easy to obtain in rigid flat sheets. The overall efficiency of the monitor depends almost linearly on the thickness of the radiator.

Even with the presence of a radiator it is still important to know the gain, and hence the threshold levels, of paddles 1 and 2 if the efficiency of the monitor is to be modeled accurately by a calculation. The gain of all the paddles can be found by noting the position of the minimum ionizing peak for an electron passing fully through the paddle. This is the reason for including the fifth paddle (paddle 0) in the design. A triple coincidence between paddles 0, 1 and 2 ensures that an electron passes fully through the veto paddle 1, and thus allows its gain to be determined.

4.1.4 Simulation Testing

Once the photon flux monitor was designed with respect to the principles behind photon counting (as described above), the response of the monitor was investigated by using a computer simulation. This was done using the GEANT4 [GEA03] toolkit and the LUCID [Mur95] data-acquisition and analysis system. GEANT simulates particles as they pass through a world built from geometrical objects. Its high precision library includes all the interactions of photons and electrons with matter so it can track a particle as it travels through a material and allow it to interact with the material via the known processes. The simulation is able to take into account the cross sections for all the interactions possible in the different types of materials included in the flux monitor design. The simulation is also able to account for the light output resulting when energy is deposited in the scintillator material. Finally the simulation can impose a threshold to determine if an output will be recorded or not.

The simulated “device” consisted in 5 plastic scintillator BC-400 paddle detectors with default dimensions of 150×100 mm (with an average thickness of 2.1 mm). Between the second and the third paddle detector, in the direction of the beam line, an Al plate was inserted (with default dimensions of 150×100 mm), playing the role of the radiator. The spacing between all paddles

was initially set at 10 mm. The entire device was positioned in air, symmetrically about the photon beam line as shown in Figure 4.2. With these dimensions the centering of a typically 1 inch (25.4 mm) diameter photon beam on the monitor is not critical.

The simulation showed that the efficiency of the flux monitor depends weakly on construction dimensions such as the width and height of the paddles, the spacing between the paddles and the thickness of the scintillator material in the paddles. The strongest dependence was on the thickness of the aluminum radiator. A radiator thickness of 2 mm was chosen as being thick enough so that the monitor efficiency weakly depends on discriminator threshold levels while keeping the overall efficiency below about 2%. With this thickness a change of 10% in the discriminator level of paddle 1 or paddle 2 resulted in less that a 0.5% change in the efficiency of the monitor.

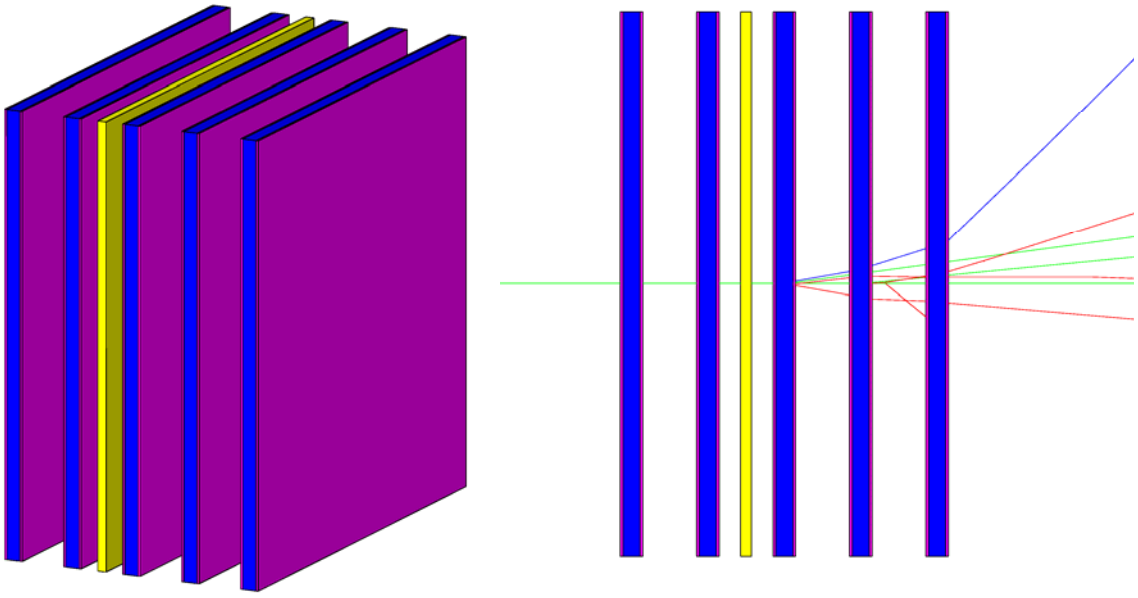

a) b)

Figure 4.2 a) The photon flux monitor's geometry generated by GEANT4 (diagrams courtesy of W. Wurtz); b) Simulation of events (20 photons of 20 MeV) generated by GEANT4 (Green trajectories are for neutral particles, including photons, red for positively charged particles and blue lines are for negatively charged particles)

Figure 4.3 shows the predicted efficiency for the monitor as a function of energy. It can be seen that the monitor will be usable over a wide energy range.

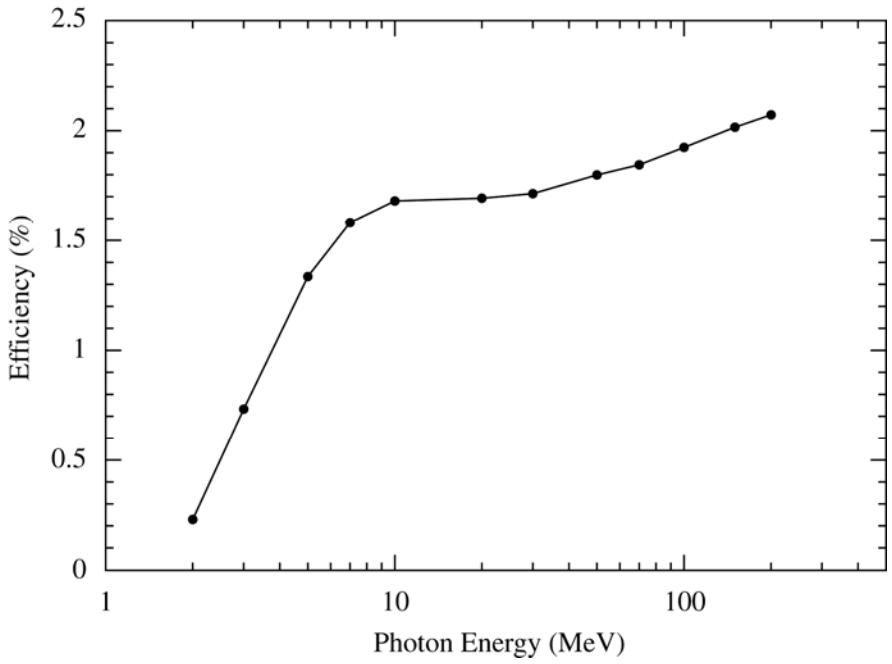

Figure 4.3 The efficiency of the flux monitor, as calculated using the GEANT4 simulation, is plotted as a function of photon energy. The uncertainties in the calculated points are smaller than the plot symbols.

An example of the calculated spectra from the paddles is shown in Figure 4.4. Shown are the spectra for paddles 2, 3 and 4 when a triple coincidence between them and no signal from the veto paddle 1 is required. Two peaks can be seen in the spectra. The lower energy one corresponds to the minimum ionizing peak for a photoelectric or Compton electron. The higher energy one corresponds to the double minimum ionizing peak for an electron and positron pair passing through the paddle. The effect of the discriminator threshold can be seen for paddle 2, but it can be seen that the spectra for paddles 3 and 4 are well above the discriminator threshold. Therefore, even for paddle 2, most of the spectrum is above the discriminator threshold. Therefore small changes in gain of any paddle will have little influence on the total number of counts.

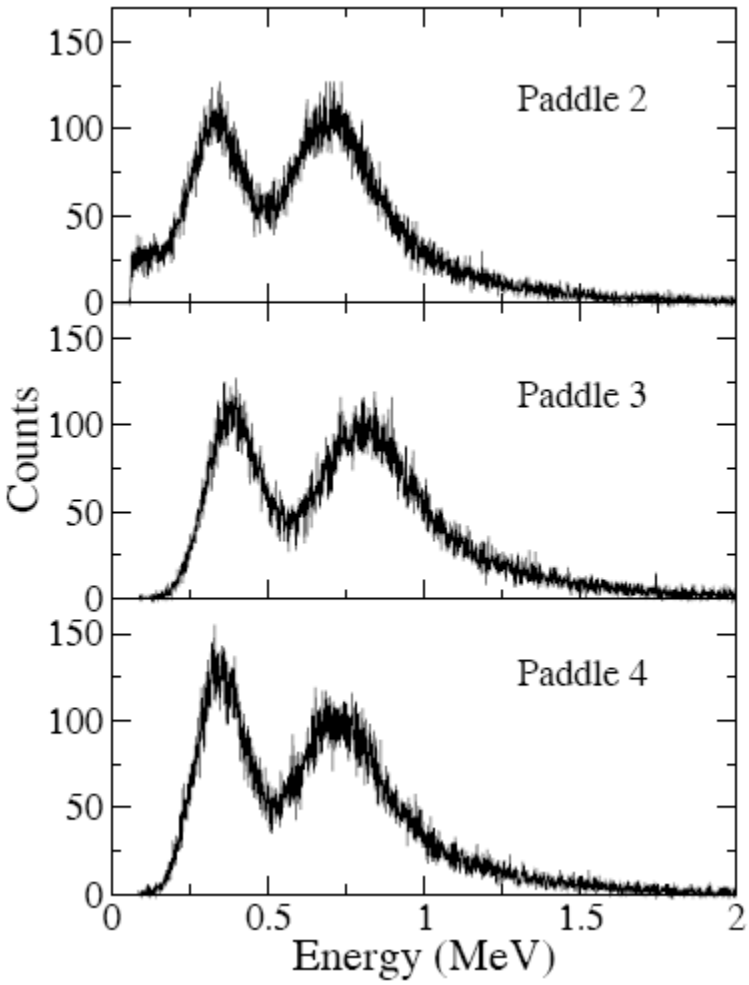

Figure 4.4 Paddle spectra calculated from the simulation for a photon energy of 30 MeV. The spectra shown are for the condition of a triple coincidence between paddles 2, 3 and 4 and no hit in the veto paddle 1. Note that the energy of the minimum ionizing peaks for each paddle are at slightly different energies since the paddles have slightly different thicknesses

4.2 Flux Monitor Construction

The complete flux monitor was constructed using some available components at the Department of Physics and Engineering Physics at the University of Saskatchewan.

The 2.1 mm thick 150 mm × 100 mm BC-400 (Table 4.1) sheets are coupled to a phototube via adiabatic Lucite light guides attached to one of the 10-cm long edges. Philips XP2012 (Table 4.2

and Figure 4.5), Standard, 10 stage, 39 mm diameter phototubes were used as these were readily available. The scintillator, light-guide and phototube assemblies are clamped in an aluminum frame so that the scintillator paddles are spaced 28.5 mm apart. Between paddles 1 and 2, a frame allows the mounting of various thickness radiators. For the tests described in this thesis an aluminum radiator of thickness about 2.3 mm was used.

Table 4.1 Some properties of BC-400

Light Output, % Anthracene	65
Refractive Index	1.58
Light Attenuation Length, cm.	160
Wavelength of Max. Emission, nm.	423
No. of H atoms per cm^3	5.23×10^{22}
No. of C atoms per cm^3	4.74×10^{22}
Ratio of H:C	1.103
No. of electrons per cm^3	3.37×10^{23}
Softening Point	70^0 C
Radiation detected	> 5 MeV gamma rays
Principal uses/application	General purpose

Table 4.2 Some characteristic of the 10-stage, 39 mm, round PMT tube Philips XP2012

Window material	Lime-glass
Photocathode	Bi-alkali
Refractive index at 420 nm	1.54
Gain	6.5×10^5
Anode pulse:	
Rise time	3 ns
Duration at half-height	7 ns
Transit time	28 ns
Spectral range	290-650 nm
Maximum sensitivity	420 nm

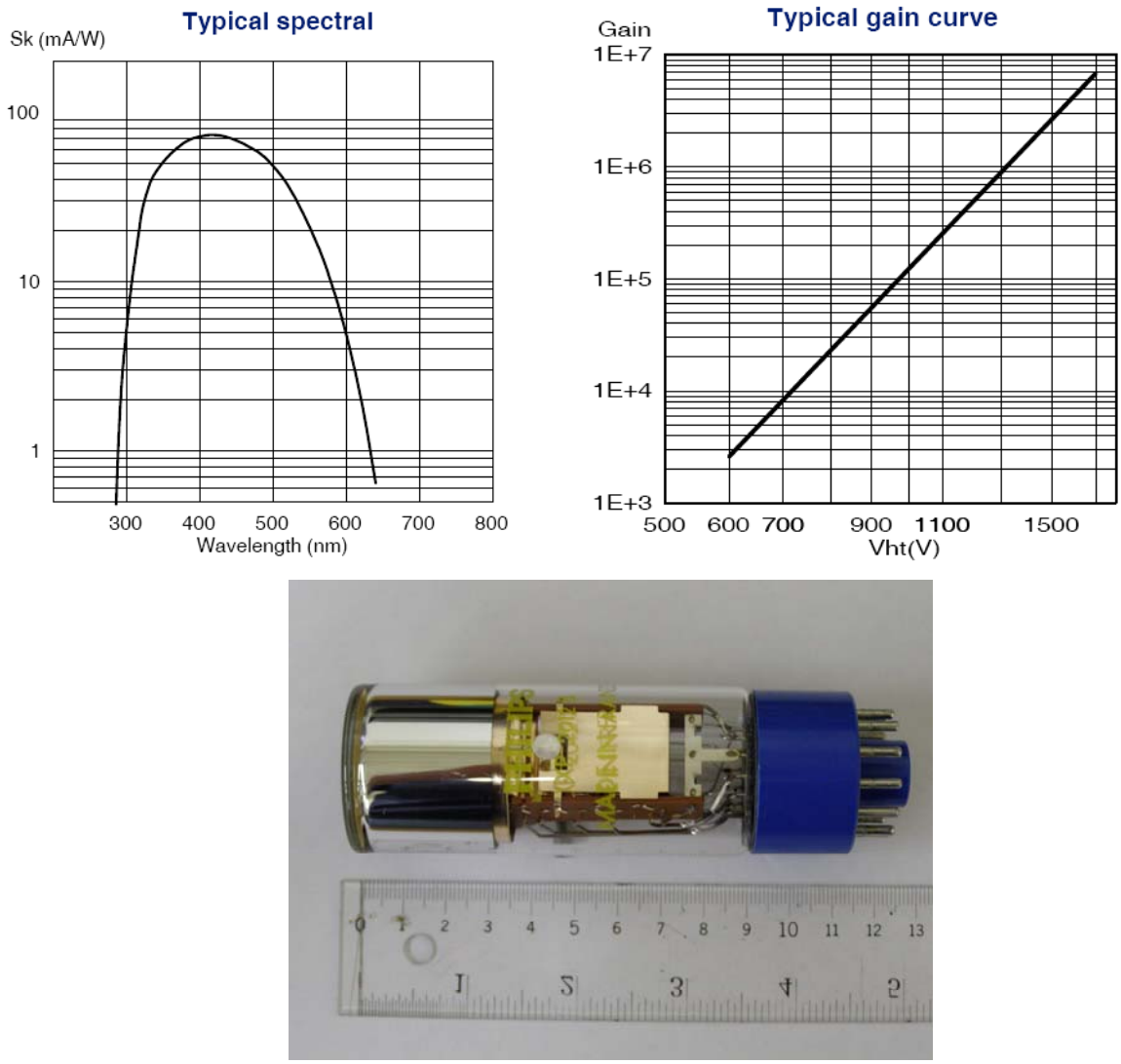

Figure 4.5 The Philips XP2012 PMT with a few characteristics (feature graphs from Photonis Group PMT catalogue; image taken in the Physics lab)

The casings for the PMTs were completely redesigned as the configuration used in a previous project was unsuitable for this application.

QCad drawings and pictures are presented in Figure 4.6, a) and b), and Figure 4.7. All the components were manufactured at the Physics machine shop (Figure 4.8).

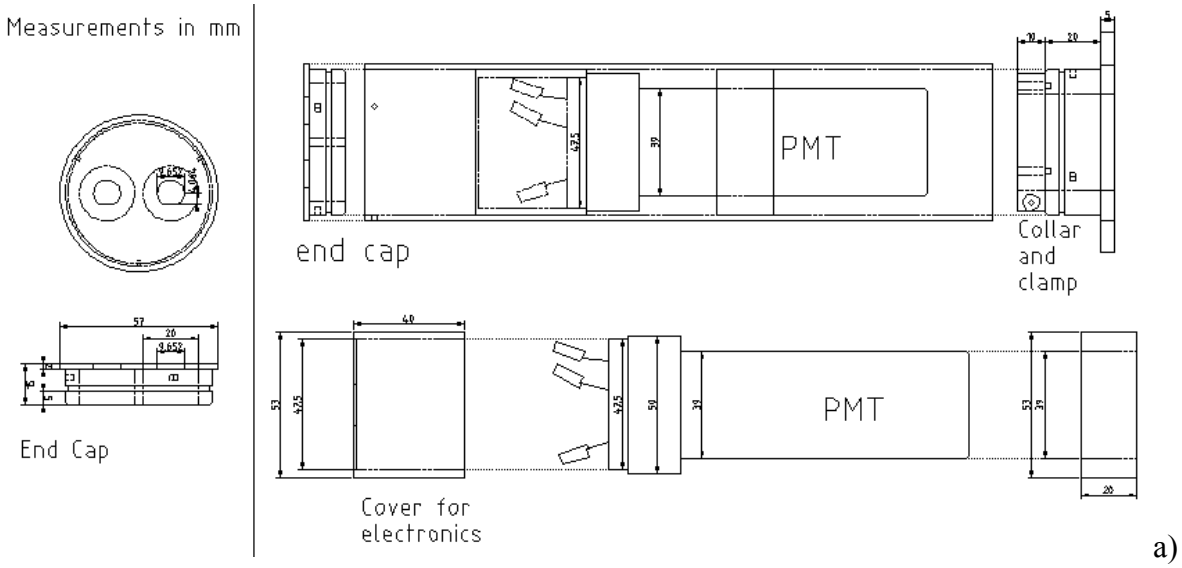

a)

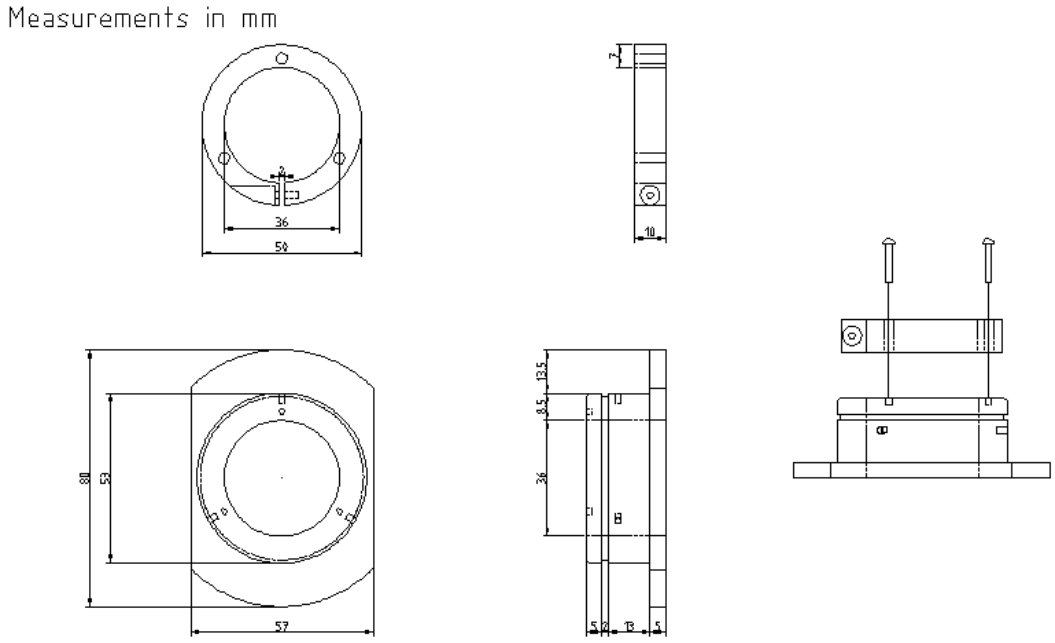

b)

Figure 4.6 a) QCad drawings for the casing of the PMT, collar and clamp, b) Cover for the electronics and the end cap

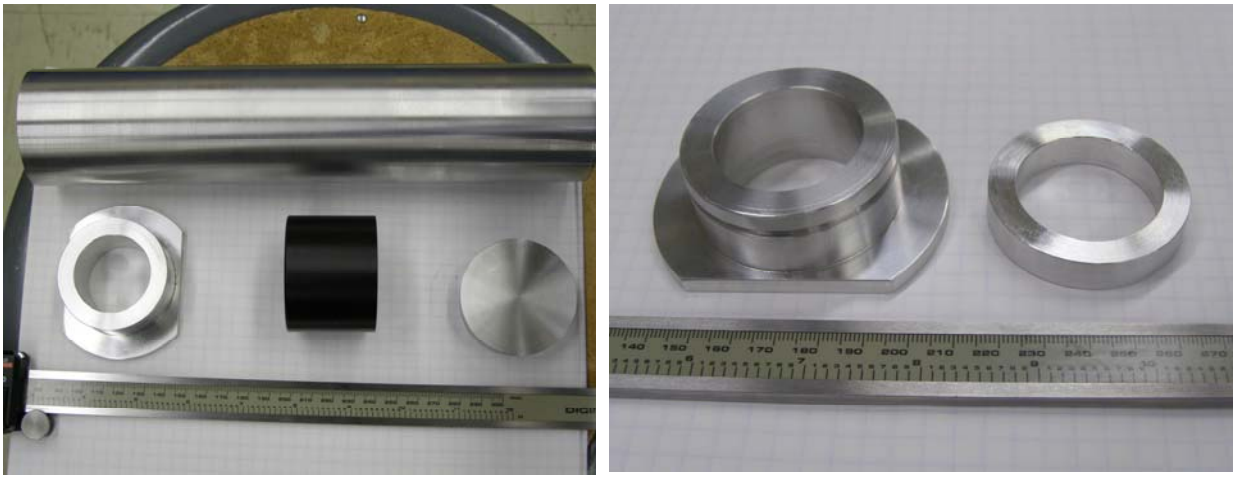

Figure 4.7 New PMT's casing with the collar and clamp (for the front end) and end cap. Made of Delren (electrically nonconductive plastic), in the left picture, is the protective collar for the PMT

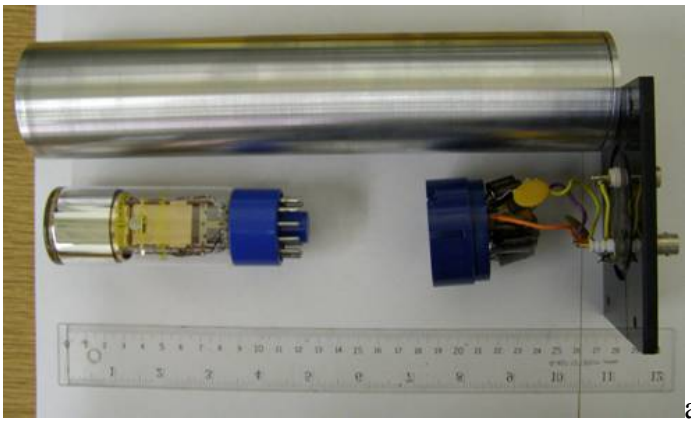
a)

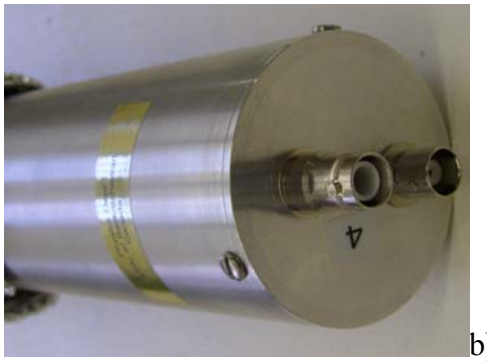
b)

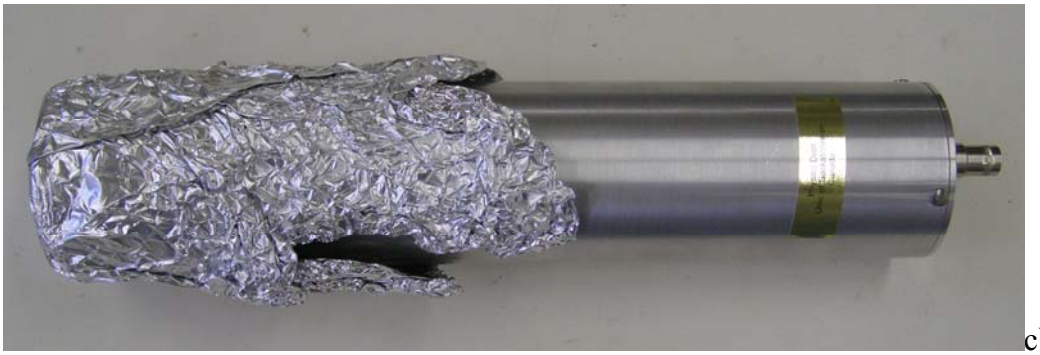
c)

Figure 4.8 a) The PMT with its electronic base and its new casing; b) End cap of the PMT's casing; c) Complete PMT

The light guides were designed from scratch specifically for this project. The drawing provided to the Physics machine shop is given in Figure 4.9. The light guides are manufactured from Lucite - polymethylmethacrylate $(C_5O_2H_8)_n$ - index of refraction of 1.49 - 1.51. Lucite is the most widely used material for light guides. It can be shaped quite easily into complex shapes and is produced by several manufacturers. If the machining of the Lucite (sheets and rods from Spartech Polycast) was a common job, the polishing involved after was a sensitive and time consuming work, as it had to be done manually. The polishing was made in several steps, beginning with using different sandpaper grips (320, 400 and 600, the finest) then polishing with heavy and fine scratch removers, and finally with plastic cleaner and shiner (Figure 4.10).

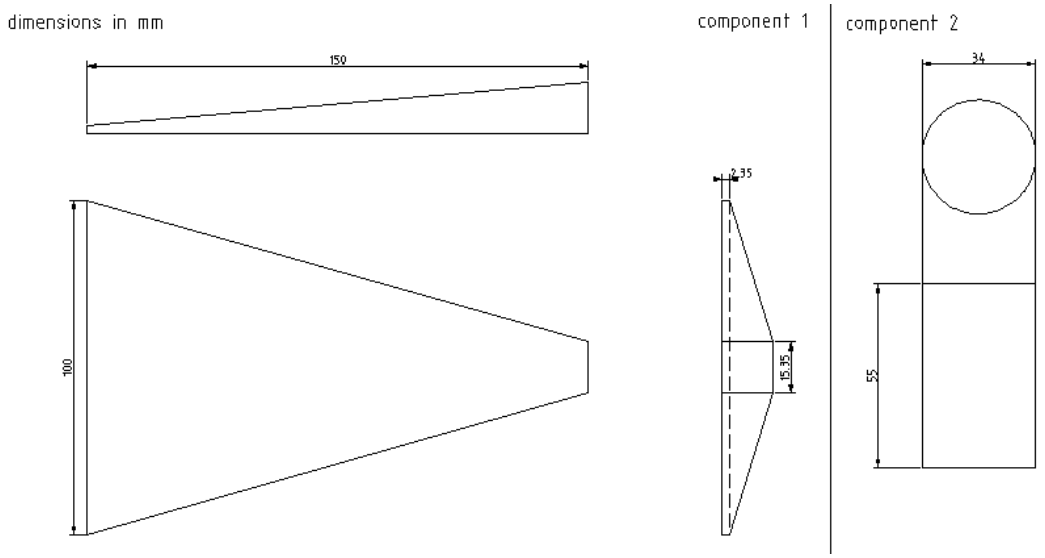

Figure 4.9 QCad drawings for the light guide

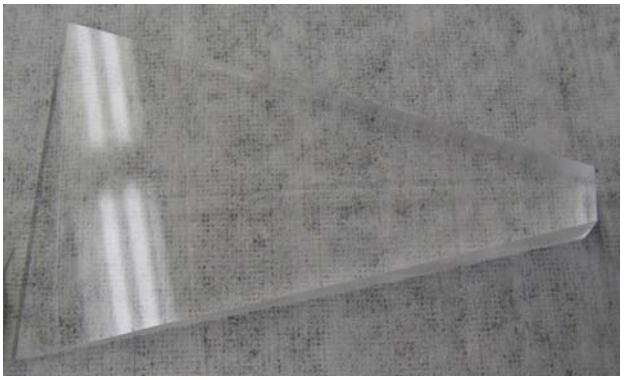

The rectangular prism part of the light guide

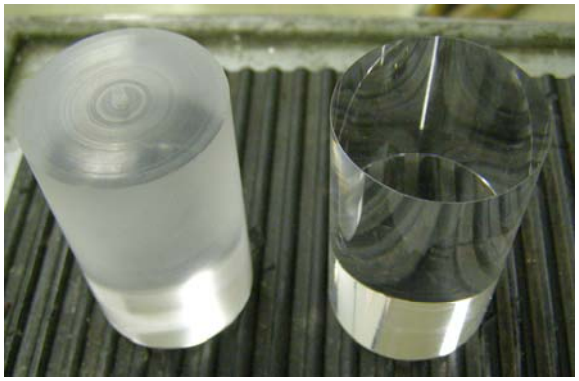

The cylinder part from the end of the light guide (left side, before polishing)

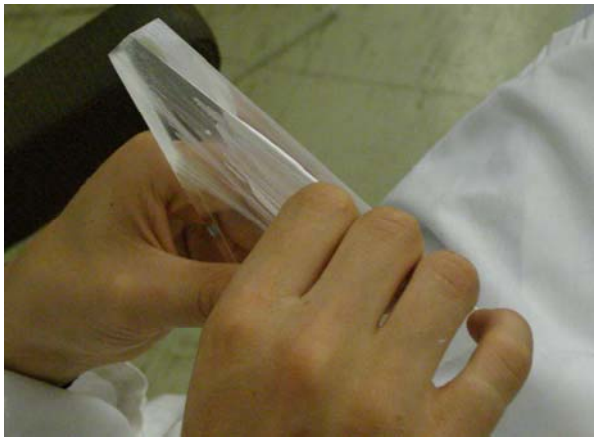

Manual polishing

Plastic scratch removers used

Figure 4.10 Different stages in the polishing process

Gluing together the scintillator plates with the light guides was the next step. The scintillator plates were first glued to the rectangular prism part of the light guide, using BC-600 Optical Cement, specifically designed for gluing scintillators (Figure 4.11). The proportions by weight for the BC-600 epoxy optical cement were 100 parts resin, 28 parts hardener. The mixture sat undisturbed for 15-20 minutes before application, in order to de-bubble the mixture. The curing time was 24 hours for each glued surface.

After complete curing of the scintilator paddle with the rectangular prism, the bottom portion of the light guide was glued (this time using a fast curing WELDON 4 optical cement for joining acrylic) to the cylinder part which comes in contact with the PMT's photocathode window (Figure 4.12). A complete scintillator paddle coupled with the light guide is shown in Figure 4.13.

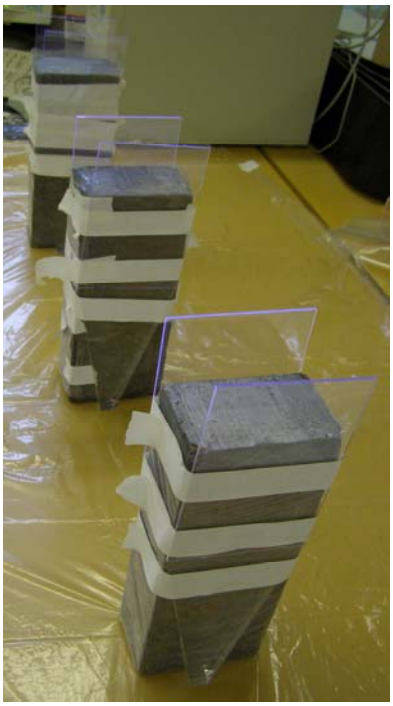

Figure 4.11 Scintillator plates waiting to cure

Figure 4.12 The two parts of the light guide glued together

Figure 4.13 Complete scintillator paddle coupled with the light guide

After complete curing, the paddles were wrapped in aluminized mylar (thickness of 0.01 mm) to help reflect light that is not reflected by total internal reflection. Mylar is the trade name of biaxially-oriented polyethylene terephthalate (boPET) polyester film and has been developed since the mid-1950s, originally by DuPont and Imperial Chemical Industries (ICI). Mylar can be aluminized by evaporating a thin film of metal onto it. Aluminized mylar reflects up to 99% of

light, including much of the infrared spectrum. A layer of black plastic (thickness of 0.25 mm) and electrical tape was added, sealing the paddle from ambient lighting (Figure 4.14).

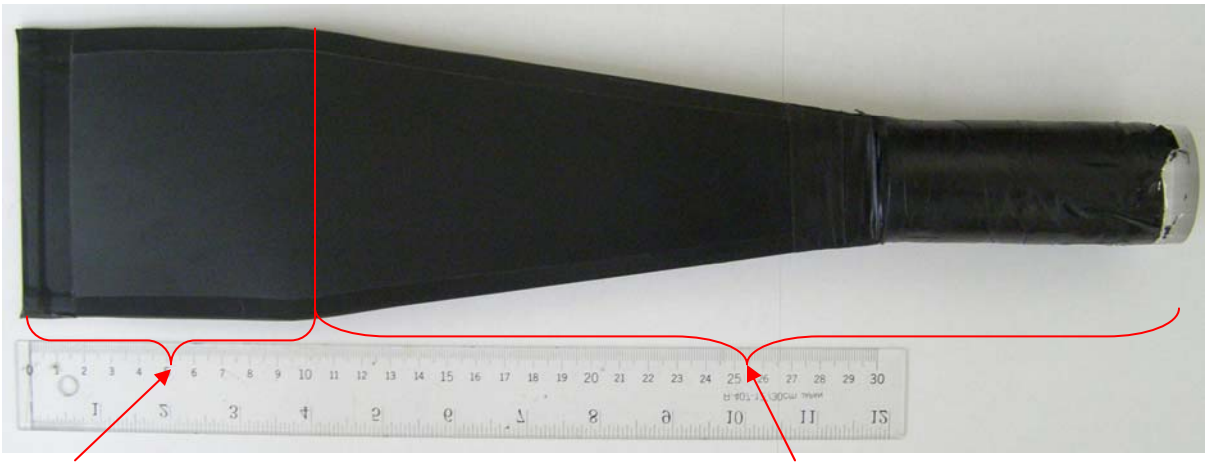

Figure 4.14 A complete scintillator paddle covered with plastic and black tape

After finishing the work on the scintillator paddles and the PMTs with their new casings, focus was oriented towards building the frame for the entire flux monitor. The frame (211 × 470 × 180 mm, with a thickness of the wall of ~ 10 mm), completely designed by our research group, is made of aluminum (Al6061) and it is shown in Figure 4.15 and 4.16.

a)

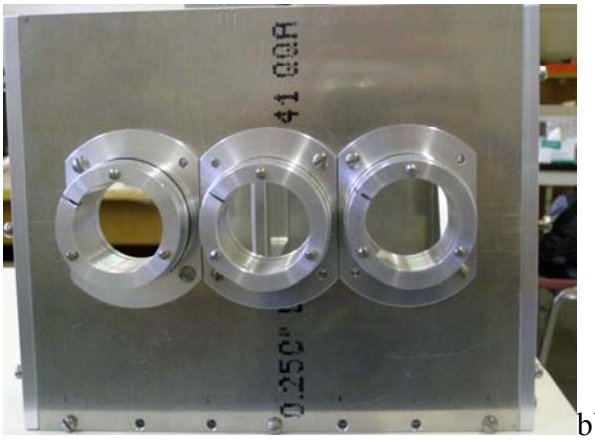
b)

c)

Figure 4.15 a) The entire aluminum frame; b) One side of the frame, with the collars for three PMTs; c) The opposite side of the frame, with collars for two PMTs

Figure 4.16 The paddles and the PMTs mounted on the frame

After testing for light leaks, and checking the light output signals from each detector individually, using a radioactive source (Ru-106 with an activity of 100 μCi), the device was shipped (each component wrapped separately for protection) to the HIGS in North Carolina.

Chapter 5

Performance Tests and Results

5.1 Calibration Runs

At HIGS, after assembly, the monitor's detectors were again tested for required function. Detector signals were scrutinized for signs of electronic noise, and again for possible holes in the light-tight wrapping. Testing also included the assignment of each detector's threshold, which must be high enough in order to filter out electronic noise, yet low enough to ensure that any signal produced by recoiling electrons or positrons is detected. Testing of the thresholds was accomplished by detecting cosmic rays.

The aluminum radiator was removed and the paddle assembly was placed on its side (Figure 5.1). A coincidence between all five paddles was required while the discriminator threshold for each paddle was set well above noise. The resulting spectra are shown in Figure 5.2.

The fact that the minimum ionizing peaks for the cosmic ray muons was well above the threshold levels indicated that the gain and resolution of the paddles are sufficiently good to operate in the manner necessary for the flux monitor.

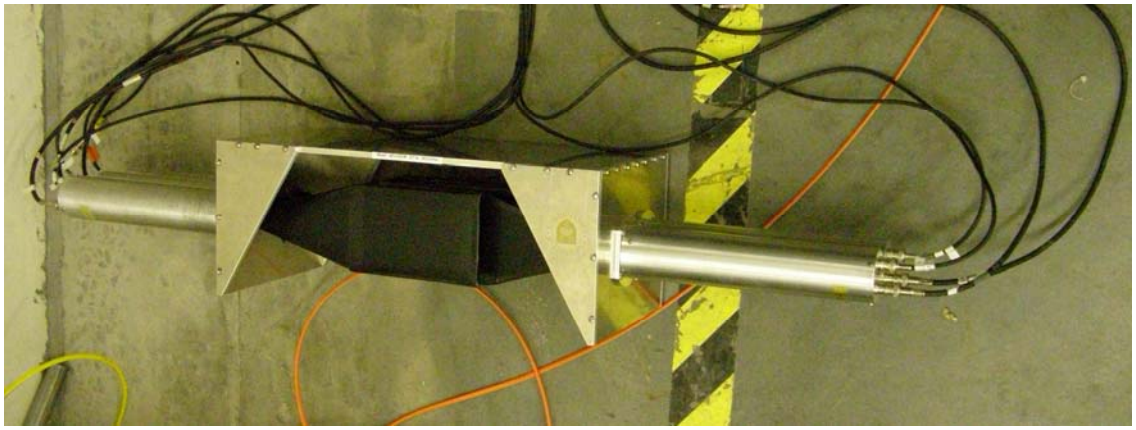

Figure 5.1 Flux monitor placed on its side in order to detect cosmic rays

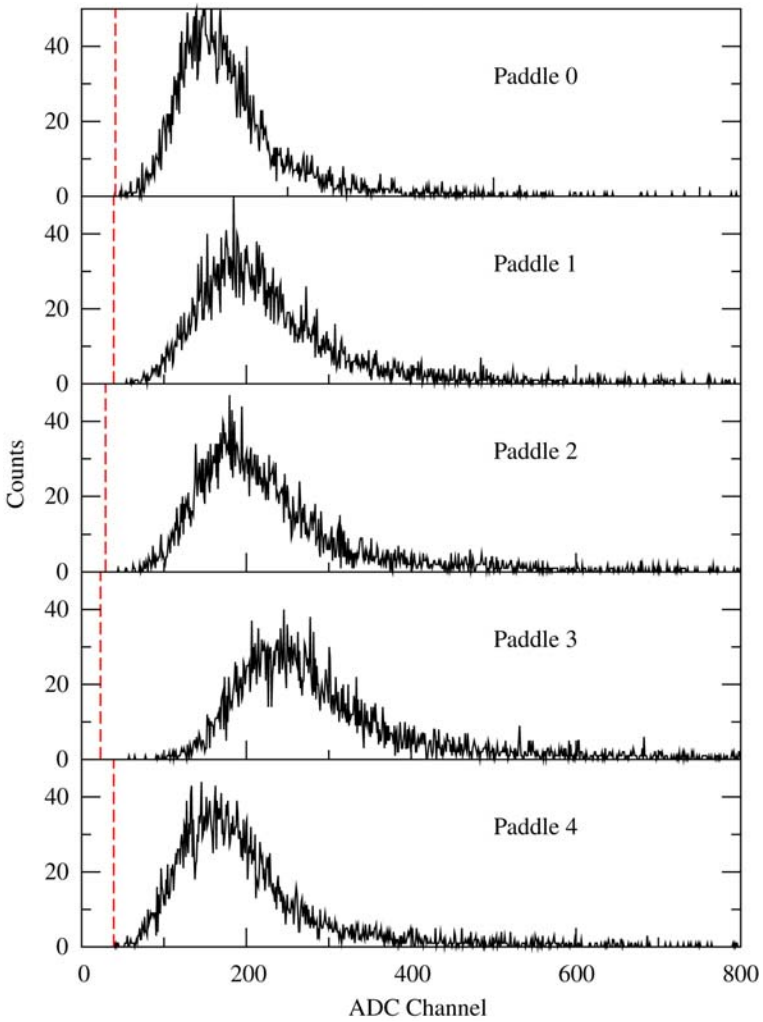

Figure 5.2 The measured spectra from the 5 paddles due to cosmic ray muons when a coincidence between all 5 is required. Dashed lines show the threshold for each paddle

Detailed tests and calibrations were carried out using the HIGS photon beam at four energies, 20, 25, 30 and 35 MeV. A schematic of the experimental arrangement used for these calibrations is shown in Figure 5.3. The electronic set-up is presented in Figure 5.4. Measurements of photo-neutrons were performed using D_2O, H_2O and empty targets, Deuterated and un-deuterated active targets, and ^6Li, ^7Li and empty targets. The photo-neutrons were detected using Blowfish. A large NaI detector was moved into the beam downstream of the flux monitor, and the photon beam intensity was reduced by inserting copper absorbers into the beam line so that the NaI would be able to count individual photons. The effect of the copper absorbers has been studied in detail by the HIGS group [Ahm07]. Each attenuator is 8.0 cm thick and the attenuator assembly is located near the exit of the storage ring, almost 50 m from the primary collimator at the entrance to the gamma vault. This distance makes changes in the room background negligible when the attenuators are inserted. The shape of the spectrum seen in the NaI detector has been observed not to change when different numbers of copper absorbers are inserted. Because of the large distance between the copper attenuators and the primary collimator even photons scattered at very small angles in the copper attenuators are removed.

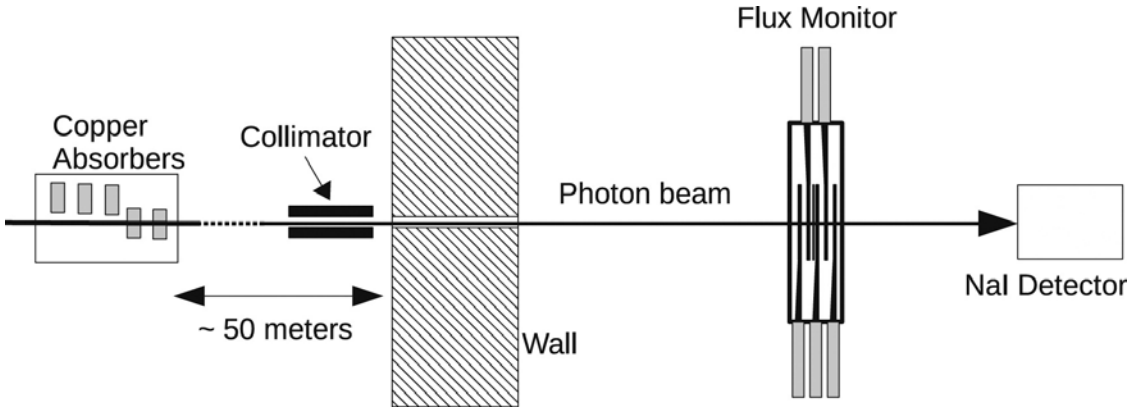

Figure 5.3 A schematic of the experimental arrangement used to characterize the photon flux monitor (not to scale).

This observation is supported by GEANT4 simulations which show that the NaI spectrum shape is unchanged when copper attenuators are inserted. The number of photons incident on the NaI detector was determined by integrating the NaI spectrum from about 9 MeV up. This removes the room background present at low energies, which is mostly natural radioactivity present even when the beam is off.

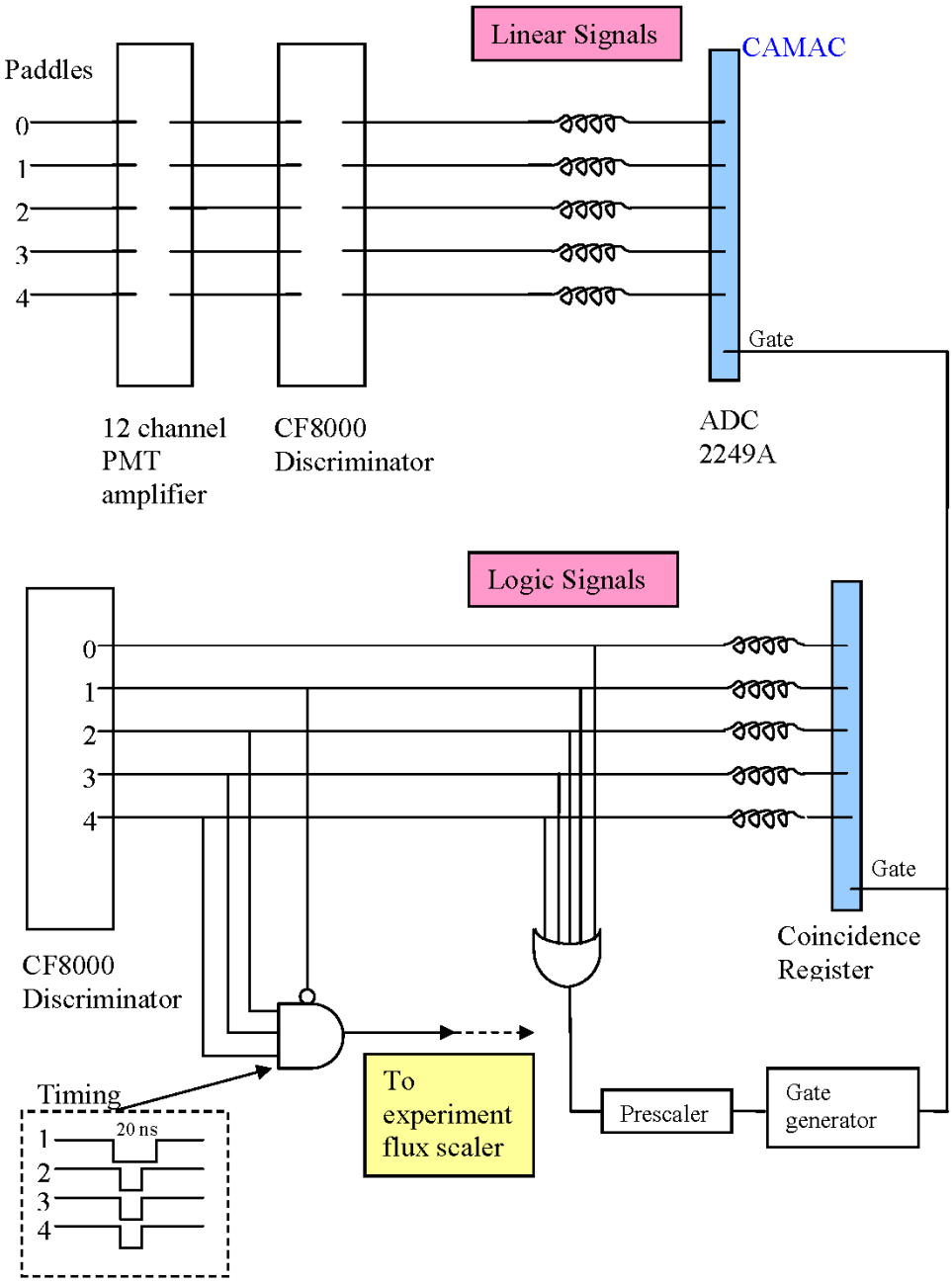

Figure 5.4 Flux monitor electronics

The signal from each paddle is split in the discriminator: one part constitutes the inputs of the Analog-to-Digital-Converter (ADC), the other part is analyzed in the discriminator. A prescaled signal present when any of the 5 paddle signals is above threshold is used to generate a gate for the ADC, and a gate for the coincidence register, which records which paddle is above threshold.

This set-up helps us in determining the threshold by accumulating histograms for each individual paddle when is above threshold. As well it gives us the chance to accumulate spectra for the normal coincidence condition. We are also able to accumulate spectra when there is a coincidence between the 0, 1, and 2 paddles, which allows us to determine the gain, and hence the energy threshold, for paddle 1.

The flux monitor runs are summarized in Table 5.1 and presented in a chronological order. Column 1 is the photon beam energy and column 2 is the LUCID data acquisition run number. Column 3 is the rate in the flux monitor scaler during the live time which is listed in column 4. Column 5 is the integral of the NaI spectrum which is recorded during the live time. An example of a NaI spectrum is shown in Figure 5.5 with the lower integration limit indicated by the vertical line. The integration omits the low energy background visible in the spectrum.

Table 5.1 Flux Monitor Calibration Runs

Beam Energy (MeV)	Run	Rate (Hz)	Live Time (s)	NaI Sum	Count
25	595	6.8	31.975	10031	217
25	663	6.7	434.5	150231	2932
25	664	72	775.03	3.115×10^6	55790
20	708	8.6	454.02	198150	3922
20	709	91	609.08	3.080×10^6	55533
35	857	19	362.89	378609	6827
35	858	265	22.24	324808	5889
20	891	11	365.73	203670	4151
20	892	75	156.48	645964	11715
25	921	6.3	1610.40	519540	10078
25	922	69	284.33	1.086×10^6	19550
30	951	7.2	126.496	42982	908
30	952	55	213.24	642477	11660
35	973	65	222.608	791070	14437

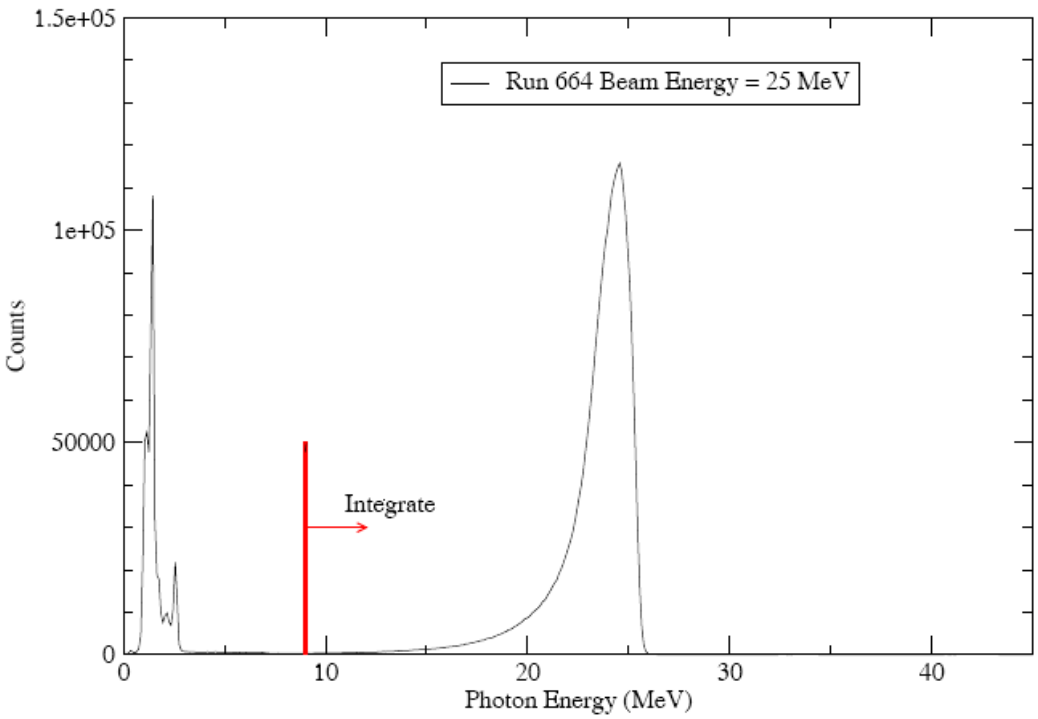

Figure 5.5 An example NaI spectrum for run number 664 at a beam energy of 25 MeV (the spectrum was integrated from 9 MeV up).

If we define, for the live time of measurement, N_γ = number of gamma rays incident on the monitor, N_m = number of measured gamma rays, i.e. the flux monitor counts, and N_{NaI} = number of gamma rays measured by the NaI detector, then we can define $\varepsilon_m = N_m / N_\gamma$ = the flux monitor efficiency, and $f_m = 1/\varepsilon_m$ = the flux monitor calibration factor, which are the quantities we desire. However, we do not measure N_γ directly but rather N_{NaI}

Therefore, to begin with, we calculate f'_m = the measured flux monitor calibration factor, using

$$f'_m = \frac{N_{NaI} - B_{NaI} T_{live}}{N_m - B_m T_{live}} \qquad 5.1$$

where, T_{live} = the live time of the measurement, B_{NaI} = the background rate in the integration region of the NaI spectrum (which was essentially zero for all runs), and B_m = the background count rate of the flux monitor.

B_m was difficult to be determined accurately. Because of the triple coincidence requirement in the flux monitor the major contribution to the background are cosmic rays incident at angles such that they pass through the three paddles while missing the veto paddle. In addition there is a contribution from the room background when random coincidences produce a count. Several measurements were made to estimate the background count rate. These measurements were necessarily made while the beam was off. It was found that different results were obtained depending on how long the beam had been off before the measurement was made. Therefore, the best estimate of the background rate was determined from a one hour run taken just after the beam was turned off. Many measurements of f'_m were made at different photon rates, i.e. with different numbers of copper absorbers in place and different accelerator beam flux setups. It was found that at very low photon rates the value of f'_m depended strongly on the value of B_m used. The value of B_m that gave the same value of f'_m for all photon rates agreed with our experimental best estimate. Using this background rate the measured calibration factors for all photon rates, calculated using equation 5.1, agreed with each other within the errors of the measurements. However, due to the uncertainty in determining the background rate, only the measurements taken at flux monitor rates greater than 25 Hz were used. At these rates a factor of two in uncertainty in B_m resulted in less than a 0.5% change in the measured flux monitor calibration factor for most measurements.

For each measurement f'_m is calculated using equation 5.1. First, a background corrected flux monitor counts was found using $N_C = N_m - B_m T_{live}$ with uncertainty $\delta N_C = \left(\left(\sqrt{N_m} \right)^2 + \left(\delta B_m T_{live} \right)^2 \right)^{1/2}$. Then, since $B_{NaI} T_{live} \approx 0$, f'_m is calculated from $f'_m = N_{NaI} / N_C$ with uncertainty $\delta f'_m = f'_m \left(\left(\frac{\sqrt{N_{NaI}}}{N_{NaI}} \right)^2 + \left(\frac{\delta N_C}{N_C} \right)^2 \right)^{1/2}$.

The results from all measurement at each energy were averaged to obtain the final value of f'_m for each energy.

Later calibration measurements than those described in this thesis use an improved technique to determine B_m. Several measurements with a range of photon rates are made and a least squares fit is used to determine f'_m and B_m. This technique was made possible by the installation of an improved selection of copper absorber thicknesses which allowed a better range of photon fluxes to be obtained without changing accelerator parameters.

5.2 GEANT4 Simulation

A simulation of the experimental arrangement including the flux monitor and the NaI detector has been developed using the GEANT4 [GEA03] toolkit. The simulation includes all dimensions and materials in the flux monitor and the NaI detector and the relative positions of these two detectors and the primary collimator. The reasonable approximation of a uniform distribution of photons over the collimator opening was assumed. The simulation includes all relevant electromagnetic and hadronic interactions at these energies. This includes photon scattering and photon interactions producing recoil charged particles in all directions. From the simulation the spectrum from the flux monitor paddles and the NaI detector can be compared to the measured values. The simulation produces event by event data which allows the spectra, after applying the experimental thresholds and coincidence requirements, to be extracted.

During each experimental run a sample of the flux monitor spectra are recorded. An ‘or’ of all 5 discriminator outputs for the 5 paddles is used to generate a gate for an ADC connected to each paddle signal. A coincidence register also records which paddles were above its discriminator threshold.

The simulation is able to very well reproduce the spectra observed in the measurement as can be seen in Figure 5.6. The figure shows the spectra from the 5 paddles of the flux monitor when a beam of energy 25 MeV passes through it. The paddles are labelled 0 to 4 with paddle 0 at the upstream end and the aluminum radiator is between paddles 1 and 2. A count from the monitor is determined by a triple coincidence between paddles 2, 3 and 4 in anti-coincidence with the veto paddle 1. In the figure the spectra for paddles 2, 3 and 4 are for the normal condition for a flux

monitor count i.e. in anti-coincidence with paddle 1. The spectra for paddles 0 and 1 are for the condition of a triple coincidence between paddles 0, 1 and 2, which is used to determine the gain of the veto paddle 1.

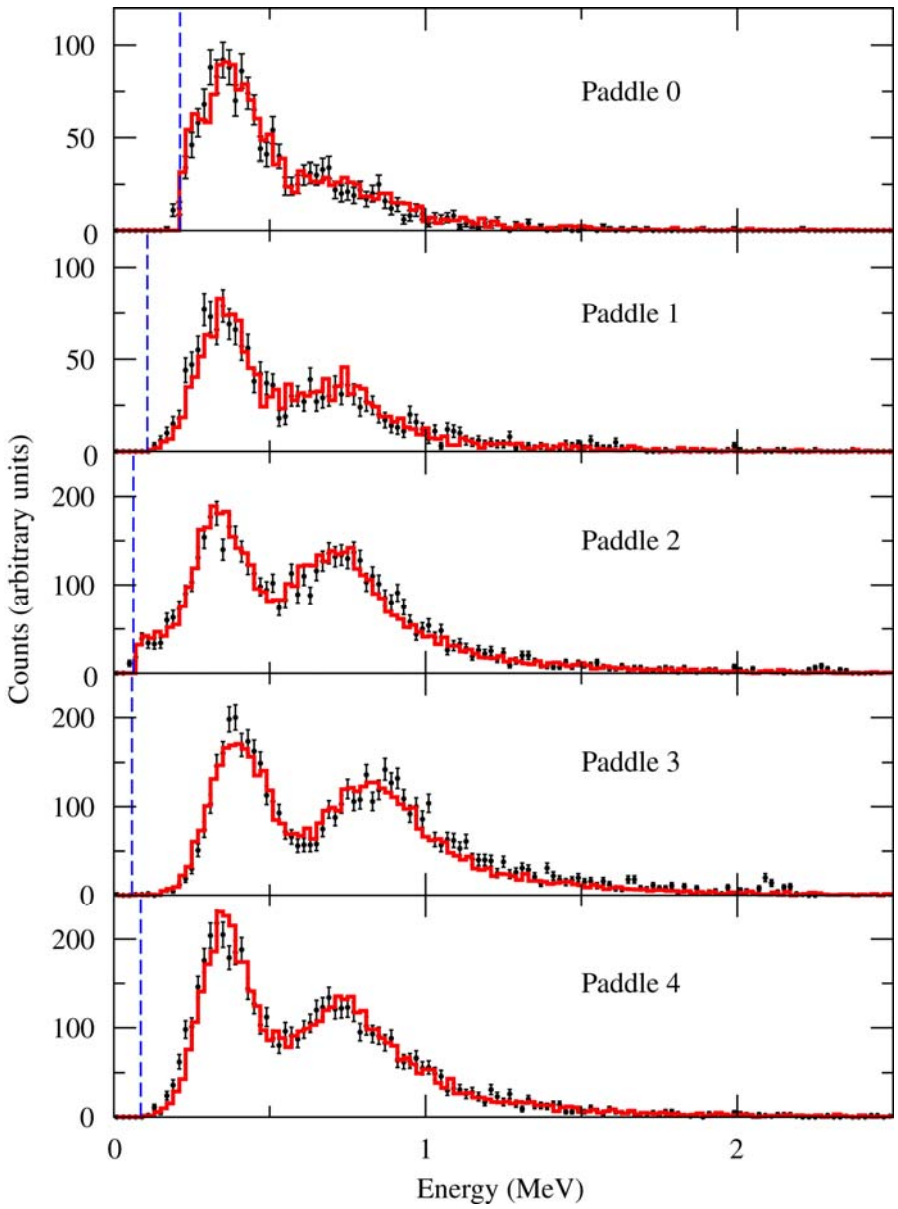

Figure 5.6 Spectra from the 5 paddles in the flux monitor compared to the simulation for a beam energy of 25 MeV. The data points are measured spectra, the solid line is the GEANT4 simulation, and the vertical dashed lines show the location of the discriminator threshold

The energy calibration for each paddle was found by matching the single minimum ionizing peak (the lowest energy peak in each spectrum) to the energy determined from the simulation. The simulated spectrum was scaled by normalizing the integral in the energy range from 0.5 MeV to 1.5 MeV to the integral of the measured spectrum.

The energy resolution of the paddles was adjusted in the simulation to match the measured spectra. It can be seen from Figure 5.6 that the shapes of the measured spectra are well reproduced by the simulation. The dashed blue lines in the figure show the discriminator thresholds for each paddle. These discriminator thresholds were determined from spectra incremented for a particular paddle with no coincidence requirement with other paddles but with the coincidence register bit set to indicate that that paddle was above its discriminator threshold.

5.3 Absorption Correction

The measured calibration factor f'_m is not equal to the true calibration factor f_m because not all gamma rays incident on the flux monitor reach, and are detected by, the NaI detector. The correction factor, defined by

$$c_{abs} = N_\gamma / N_{NaI} \tag{5.2}$$

is determined from the simulation for each energy.

The true calibration factor is given by

$$f_m = c_{abs} f'_m \tag{5.3}$$

The weighted mean of all measurements with flux monitor rates above 25 Hz was used to find the final true calibration factor. The results are summarized in Table 5.2.

Table 5.2 Measured and calculated flux monitor calibration factors for the four beam energies. Column 2 is the absorption correction factor calculated from the simulation. The uncertainty in this number is smaller than the precision quoted. Columns 3 and 4 are the measured calibration factor and efficiency after correction by the absorption factor. Column 5 is the probability of a hit in the veto (counter 1) calculated from the simulation as described in this section.

Energy (MeV)	Absorption Factor c_{abs}	Calibration Factor f_m	Efficiency ε_m (%)	Veto Efficiency ε_v (%)
20	1.0504	58.68 ± 0.50	1.703 ± 0.015	1.032 ± 0.005
25	1.0405	58.63 ± 0.50	1.705 ± 0.015	1.043 ± 0.005
30	1.0338	57.33 ± 0.51	1.745 ± 0.016	1.048 ± 0.005
35	1.0291	58.02 ± 0.43	1.723 ± 0.013	1.066 ± 0.005

The true calibration factor can also be calculated from the simulation provided all parameters of the flux monitor are known to sufficient precision. The most critical parameter in this calculation is the thickness of the aluminum radiator. The efficiency of the flux monitor is almost directly proportional to this thickness. Unfortunately this thickness is not known to sufficient precision. Micrometer measurements varied considerably.

Measurements were performed on 16 different points over the surface of the aluminum plate used as a radiator, twice at each point, using a Mitatoya digital micrometer. As the surface of the plate is far from being perfectly flat, the thickness of the radiator in the simulation was adjusted until the average efficiency for the four energies agreed with the measured average efficiency. This was achieved with a radiator thickness of 2.297 mm which was within the range of the measurements. With this radiator thickness the average measured calibration factor agreed with the average calibration factor from the simulation to within less than 0.5%. The absorption correction factors quoted in Table 5.2 are calculated using this radiator thickness.

The measured and calculated calibration factors are plotted as a function of energy in Figure 5.7.

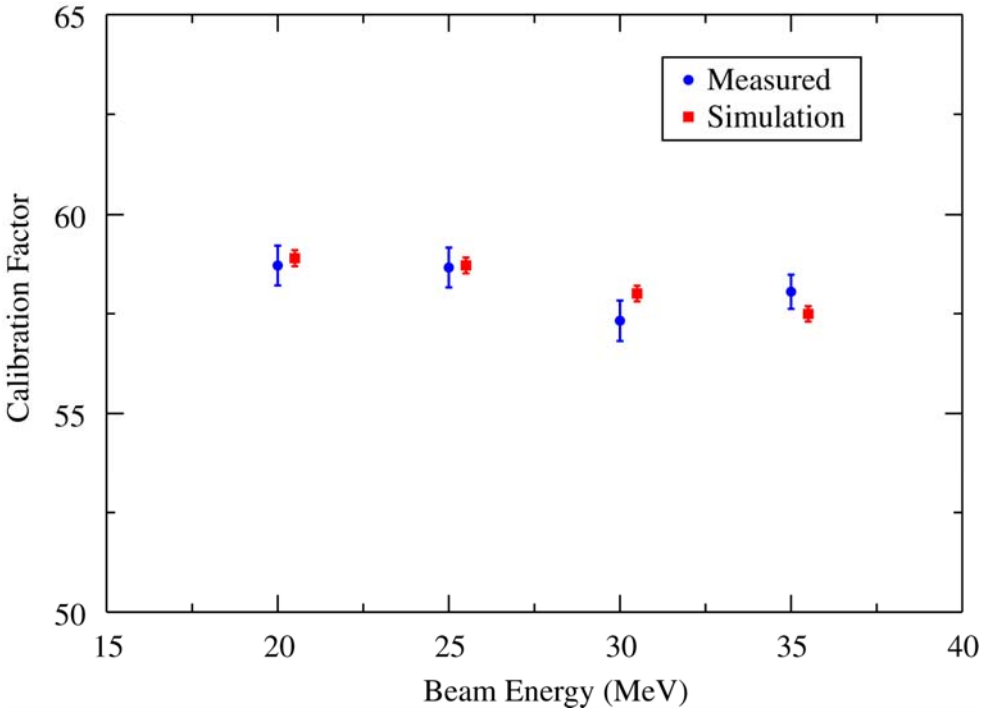

Figure 5.7 Measured calibration factors and calculated calibration factors for the 5-paddle flux monitor as a function of energy. For clarity the simulated values are offset by 0.5 MeV from the measured data points

5.4 Rate Correction

The HIGS beam is not a 100% duty factor photon beam. The photon beam comes in bunches at a rate of 5.58 MHz or about 180 ns apart. The dead-time of the flux monitor is of the order 60 ns (about the width of the veto generated by the veto paddle). Therefore photons arriving in separate bunches will always be counted by the scaler if they are detected by the flux monitor. However, more than one photon being detected in the flux monitor in a single bunch will be counted as only one.

The calibration factors were measured at very low photon fluxes so that the probability of more than one photon being detected in a single bunch is extremely small. Therefore the measured efficiency, and the efficiency predicted by the GEANT4 simulation, where one photon at a time

is simulated, is an absolute efficiency appropriate only at low rates. At high photon rates a correction for multiple hits in a bunch must be made.

The number of photons detected is reduced when two or more photons are detected in a single bunch and are counted as only one. A further reduction occurs when a photon is detected, but another photon in the same bunch causes a hit in the veto paddle, thus killing the detected photon.

Therefore in order to calculate the correction at high rates the probability that a photon hitting the flux monitor will cause a hit in the veto (paddle 1) is needed. This information can be obtained from the simulation. The results for the four energies under consideration are listed in column 5 of Table 5.2.

A full calculation of the probability of getting a count from the flux monitor in a single bunch is complicated and involves many terms. Fortunately a good approximation can be found using the following simple argument.

We define, $N_h = \varepsilon_m N_\gamma$ = the number of hits on the flux monitor that have the potential to be counted. So then, $\mu_h = N_h / B$ = the average number of hits per bunch, where B is the number of accelerator bunches during the live time of a measurement. If $P_h(x_h, \mu_h)$ is the probability of x_h hits in a bunch from Poisson statistics then, since one or more hits will be counted as one, the probability of a count will be

$$P_h(x_h \geq 1, \mu_h) = 1 - P_h(0, \mu_h) = 1 - e^{-\mu_h} \qquad 5.4$$

But this hit may be vetoed if another photon in the bunch causes a hit in the veto paddle. The probability that this occurs may be estimated as follows.

Defining $\mu = N_\gamma / B$ = the average number of photons in a bunch, then $\mu - \mu_h$ = the average number of photons in a bunch that did not cause a detectable hit. If ε_v = veto efficiency = the probability that a photon causes a hit in the veto paddle, then, $\mu_v = (\mu - \mu_h)\varepsilon_v$ = the average

number of those photons that cause a hit in the veto paddle. Therefore, from Poisson statistics, the probability that there is no hit in the veto paddle from these photons is

$$P_v(0,\mu_v) = e^{-\mu_v} \tag{5.5}$$

and therefore the total number of counts from the flux monitor is

$$N_m = BP_v(0,\mu_v)P_h(x_h \geq 1,\mu_h) = B\exp\left(-\varepsilon_v(1-\varepsilon_m)\frac{N_\gamma}{B}\right)\left(1-\exp(-\varepsilon_m\frac{N_\gamma}{B})\right) \tag{5.6}$$

This expression must be inverted to calculate N_γ from N_m. This is most easily done numerically. A first order expansion of equation 5.6 that can easily be inverted algebraically does not provide sufficient accuracy for photon rates over about 8×10^6 Hz.

The correctness of the equation for calculating N_γ was tested using Monte-Carlo simulations. In the first simulation the number of counts in the flux monitor was determined bunch by bunch. For a given photon rate, the average number of photons hitting the monitor in a bunch was calculated. For each bunch Poisson statistics was used to select a number of photons. The true efficiency of the monitor was used to randomly determine how many of these photons can cause a hit. Then the veto efficiency was used to randomly determine how many of the remaining photons caused a veto which removed the hit. After a suitable number of bunches the total number of photons hitting the monitor and the total number of counts from the monitor will be known.

In the second simulation the number of photons was again selected using Poisson statistics. Then for each photon, the actual output from a GEANT4 simulation of the flux monitor (that fired one photon at a time) was used to determine which paddles recorded hits for a given photon. An "or" of all the hit patterns in a given bunch was examined to determine if there was a hit (i.e. no hit in the veto and a triple coincidence for paddles 2, 3 and 4). Both these simulations gave the same results.

A third simulation was run using GEANT4 where multiple photons were fired in each geant event. Once again the number of photons fired was selected using Poisson statistics for a given photon rate. If the number of photons was zero the event was still recorded as a bunch.

In an actual experiment, both the total number of bunches B and the total number of flux monitor hits N_m during the live time of a measurement are recorded in scalers. Then, using the known values of the efficiencies ε_m and ε_v, the number of photons N_γ can be calculated from the last equation. This was tested, using the Monte-Carlo simulations described above, for a wide range of photon rates and the results are shown Figure 5.8. The figure shows the error in the calculated number of photons if the rate correction was ignored (i.e. if the number of photons was calculated by simply using $N_\gamma = N_m / \varepsilon_m$.)

Without a rate correction the calculated number of photons is too small, hence the negative error shown in the figure. After applying the rate correction it can be seen that equation 5.6 gives the correct number of photons to less 1%.

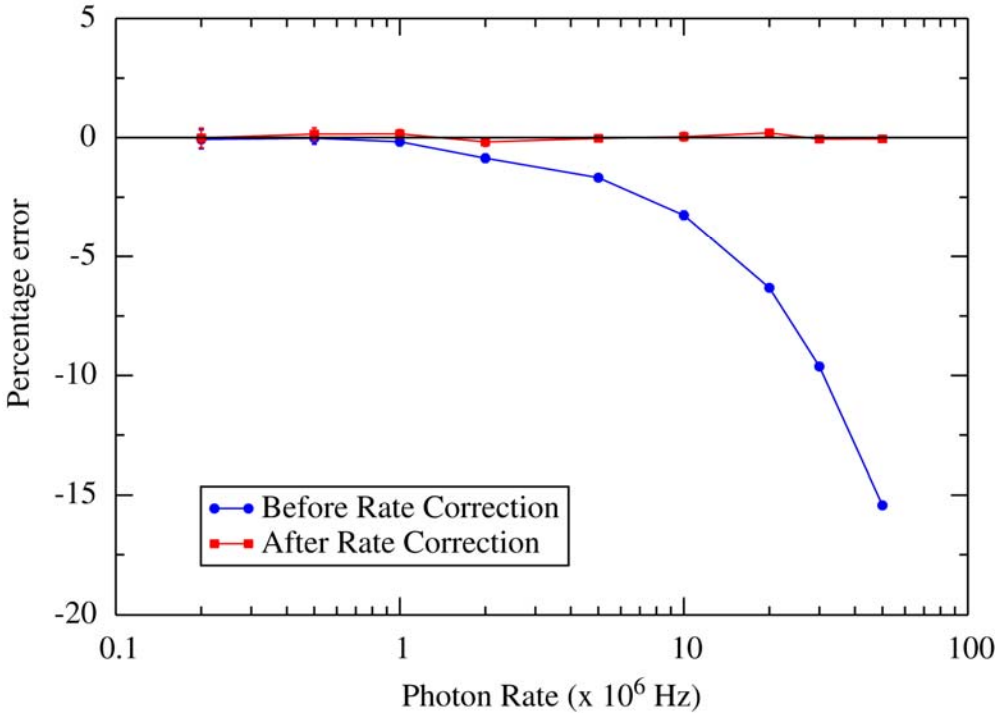

Figure 5.8 The percentage error in the number of photons as a function of photon rate. The errors without applying a rate correction and after applying a correction are shown. Uncertainties in the simulation results are smaller than the size of the data points shown

The error in N_γ depends on the uncertainties in N_m, ε_m and ε_v in the usual way,

$$\delta N_\gamma^2 = \left(\frac{\partial N_\gamma}{\partial N_m}\right)^2 \delta N_m^2 + \left(\frac{\partial N_\gamma}{\partial \varepsilon_m}\right)^2 \delta \varepsilon_m^2 + \left(\frac{\partial N_\gamma}{\partial \varepsilon_v}\right)^2 \delta \varepsilon_v{}^2 \qquad 5.7$$

in which the coefficients can be estimated from a leading order approximation of equation 5.6.

To second order, if $\varepsilon_v N_\gamma / B$ and $\varepsilon_m N_\gamma / B$ are small, equation 5.6 can be written

$$\frac{N_m}{B} = \left(1 - \varepsilon_v (1-\varepsilon_m)\frac{N_\gamma}{B}\right)\left(\varepsilon_m \frac{N_\gamma}{B} - \frac{\varepsilon_m^2 N_\gamma^2}{2B^2}\right) \qquad 5.8$$

In the form of a quadratic equation this is

$$\left(\frac{N_\gamma}{B}\right)^2 - \frac{1}{\varepsilon_v(1-\varepsilon_m)+\varepsilon_m/2}\left(\frac{N_\gamma}{B}\right) + \frac{1}{\varepsilon_m\left(\varepsilon_v(1-\varepsilon_m)+\varepsilon_m/2\right)}\left(\frac{N_m}{B}\right) = 0 \ ,$$

$$\text{or } \left(\frac{N_\gamma}{B}\right)^2 - \frac{1}{\varepsilon'}\left(\frac{N_\gamma}{B}\right) + \frac{1}{\varepsilon'\varepsilon_m}\left(\frac{N_m}{B}\right) = 0 \qquad 5.9$$

where $\varepsilon' = \varepsilon_v(1-\varepsilon_m) + \varepsilon_m/2$. The solution of this is

$$\frac{N_\gamma}{B} = \frac{1}{2}\left[\frac{1}{\varepsilon'} \pm \sqrt{\frac{1}{\varepsilon'^2} - \frac{4}{\varepsilon'\varepsilon_m}\frac{N_m}{B}}\right] \qquad 5.10$$

which can be written

$$\frac{N_\gamma}{B} = \frac{1}{2\varepsilon'}\left[1 - \sqrt{1 - \frac{4\varepsilon'}{\varepsilon_m}\frac{N_m}{B}}\right] \qquad 5.11$$

where we have noted that the negative square root is the correct solution.

We note that

$$\frac{4\varepsilon'}{\varepsilon_m}\frac{N_m}{B} \sim 4\varepsilon'\frac{N_\gamma}{B} < 1 \qquad 5.12$$

since $N_\gamma / B \sim 1-10$ and $\varepsilon' \sim 0.02$.

Making use of $(1-x)^{1/2} \approx 1 - 1/2x - 1/8x^2$ it can be shown that

$$\frac{N_\gamma}{B} = \frac{1}{\varepsilon_m}\frac{N_m}{B} + \frac{\varepsilon'}{\varepsilon_m^2}\left(\frac{N_m}{B}\right)^2 \qquad 5.13$$

So finally

$$N_\gamma = \frac{N_m}{\varepsilon_m} + \frac{\left(\varepsilon_v(1-\varepsilon_m)+\varepsilon_m/2\right)}{\varepsilon_m^2}\frac{N_m^2}{B} \qquad 5.14$$

The leading order term is as expected if there is no rate correction.

Taking the partial derivatives of this expression leads to the following coefficients

$$\frac{\partial N_\gamma}{\partial N_m} = \frac{1}{\varepsilon_m}\ ,\ \frac{\partial N_\gamma}{\partial \varepsilon_m} = -\frac{N_m}{\varepsilon_m^2}\ \text{, and}\ \frac{\partial N_\gamma}{\partial \varepsilon_v} = \frac{(1-\varepsilon_m)^2 N_m^2}{\varepsilon_m^2 B} \qquad 5.15$$

For the partial derivatives with respect to N_m and ε_m we have used only the leading order term.

5.5 Other Rate Effects

Figure 5.9 shows the spectra from the flux monitor paddles at different rates. The spectra at a beam energy of 25 MeV taken at a very low photon rate is compared to the spectra taken at a rate of about 9×10^6 Hz.

The gain of the paddles does not appear to change much with rate. Since the efficiency is only weekly dependent on gain this will have little effect on the efficiency of the monitor. There seems to be a decrease in resolution for some paddles, especially visible at low pulse heights. This appears to be associated with the gating of the ADC. This is confirmed by effects observed in the pedestals for the ADC for those paddles.

An additional confirmation that the effect is related to the ADC comes from the fact that there appears to be counts in the spectra below the pedestal level. This would not be possible if the change in the signal occurred before it reached the discriminator. Therefore, the flux monitor scaler counts are unaffected by these effects observed in the spectra.

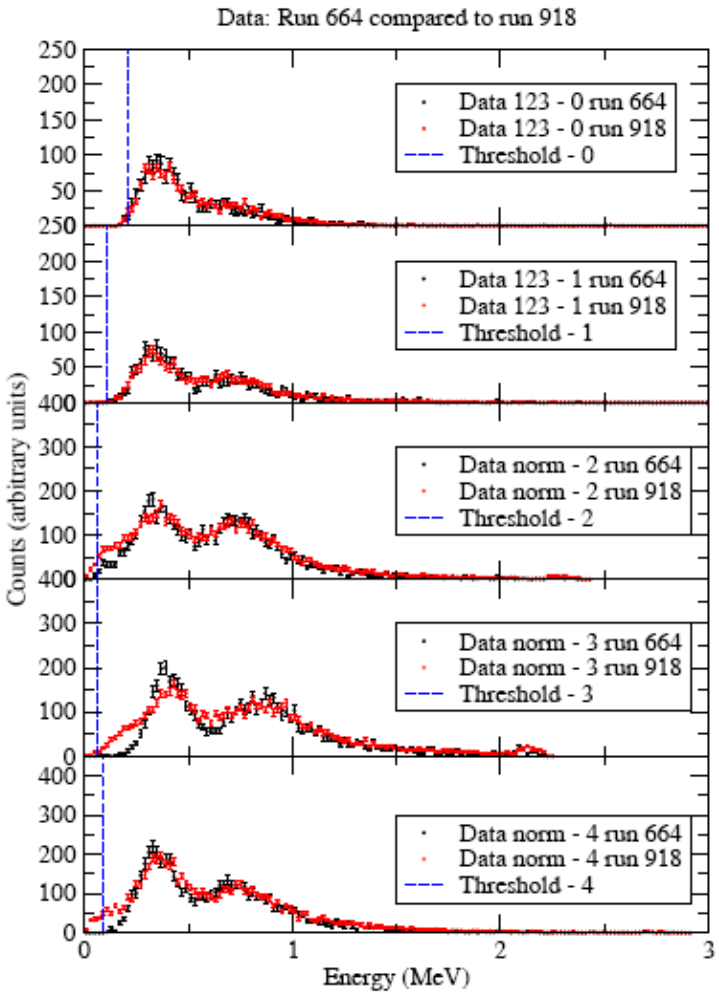

Figure 5.9 The spectra taken at different photon rates. Run 664 is at a very low rate while run 918 is at a rate of about 9×10^6 Hz

An increase in the background singles rate in the veto paddle at high beam fluxes would potentially decrease the efficiency of the flux monitor. This would have to be room background from other sources than the photons passing through the monitor which are already taken into account. Additional room background is a possibility since background rates change as a function of time after the beam was turned off. However, there is no evidence that such a background is very large and the efficiency of a single paddle to background is small since the paddles are thin. This effect is something that should be confirmed in the future by moving the flux monitor out of the beam. If the rate of such background is less than 10 MHz the effect on the efficiency of the monitor will be less than 0.5 %. In practice an estimate of ε_v can be

experimentally determined for each run since scalers record the counts from the veto paddle along with the total flux monitor counts N_m.

5.6 Target Absorption

The number of gamma rays calculated above is the number hitting the flux monitor, not the number entering the target, which is generally the quantity required for determining a reaction cross section.

There are two ways to deal with this. One is to run the flux monitor GEANT4 simulation again with a target in place. Then the values of ε_m and ε_v derived from the simulation will include target absorption effects and the number of gamma rays derived using the above procedure will be the number entering the target. This is the preferred approach since the simulation will also allow a correction to the measured cross section due to photon absorption in the target.

However, a first approximation correction can be made using the mass attenuation coefficient μ/ρ of the target for the gamma ray energy in question. The absorption coefficient is $\mu = (\mu/\rho)\rho$ where ρ is the density of the target. If the target thickness is t and the number of gamma rays entering the target is $N_{\gamma 1}$, the number of gamma rays leaving the target is

$$N_\gamma = N_{\gamma 1} e^{-\mu t} \tag{5.16}$$

When calculating the cross section for a reaction it is important to include absorption along the length of the target. This is best accounted for by using a simulation. A first approximation can be made using the following analysis. The number of gamma rays passing through a part of the target which is a distance x from the start of the target is

$$N_\gamma(x) = N_{\gamma 1} e^{-\mu x} \tag{5.17}$$

The number of nuclear reactions, with cross section σ, that occur in a piece of target of thickness Δx at a distance x from the start of the target is

$$N_R(x) = N_\gamma(x) n \sigma \Delta x \tag{5.18}$$

where n is the number density of reaction centres in the target. The total number of reactions that occur in a target of thickness t is then

$$N_R = \int_0^t N_\gamma(x) n \sigma dx \qquad 5.19$$

Using equation 5.17 we find

$$N_R = N_{\gamma 1} \frac{n\sigma}{\mu}(1 - e^{-\mu t}) \qquad 5.20$$

And then using equation 5.16 we get

$$N_R = N_\gamma \frac{n\sigma}{\mu}(e^{\mu t} - 1) \qquad 5.21$$

5.7 Stability

The photon flux monitor must have a stable efficiency over a wide range of photon intensities. Therefore the gain of each paddle must be stable so that the discriminator threshold level is stable. Although the monitor has been designed to be relatively insensitive to small changes in gain, it is important to monitor the gains during an experimental measurement. If changes in gain are observed a correction to the efficiency of the monitor can be calculated using the simulation.

As mentioned in section 5.2, a pre-scaled sample of the spectra from each paddle is recorded during each experimental run. By observing the location of the single and double minimum ionizing peaks in these spectra the gain of each paddle may be determined and changes in this gain may be tracked.

During experimental runs at HIGS, at photon rates of up to 3×10^7 Hz, no significant changes in gain were observed. This may be due in part to the fact that the count rate from the monitor is effectively limited by the bunch rate from the accelerator of 5.58 MHz, and therefore events in each paddle are, in general, at least 180 ns apart.

Chapter 6

Conclusions and Future Work

A photon flux monitor for the High Intensity Gamma Source at the Duke University Free-Electron Laser Facility has been developed. Its response is well characterized by a GEANT4 simulation. The simulation is able to very well reproduce the spectra observed in the measurement, as presented in Section 5.2. It has been shown to be stable over a wide range of photon intensities up to 3×10^7 photons/s. During experimental runs at HIGS no significant changes in gain were observed (Section 5.7).

It may be accurately calibrated against a NaI detector at low photon rates (Section 5.1) and corrections needed at high photon rates are easily and accurately calculable (Sections 5.3, 5.4, 5.5 and 5.6). Results of measurements and calculations required to characterize the 5-paddle photon flux monitor were presented and discussed.

Using the correct thickness for the radiator, the simulation agrees with the measured efficiency. That gives us confidence that we can use this simulation to predict the behaviour of the photon flux monitor in other situation. However, there always remain the necessity of calibrate the photon flux monitor for each simulation and for each energy used.

We can conclude that the monitor, after proper calibration, and after correction for rate effects, easily achieves its design goal of measuring the number of photons incident upon it during the live time of a measurement to at least the 2% accuracy needed for precision photonuclear reaction measurements. [Pyw09]

Future work will include verifying the operation of the flux monitor over a wider range of photon energies than those discussed in this thesis. As well an experimental confirmation of the rate correction describe in Section 5.4 would be desirable. Also, the effect of additional room background is something that should be thoroughly checked in the future by moving the flux monitor out of the beam.

References

[Ahm07] M.W. Ahmed, R.M. Prior1, and H.R. Weller, *γ-Ray Beam Flux Monitoring with Improved Scintillator Paddles*, Communication at Duke University, TUNL Progress Report 46, 2007, Page 104.

[Ant91] I. Anthony, J.D. Kellie, S.J. Hall, G.J. Miller, and J. Ahrens, *Nucl. Inst. and Meth., Section A, Vol. 301*, 1991, Pages 230-340.

[Arm00] John C. Armitage et al., Charged Particle Measurement, CRC Press LRC, 2000.

[Bew05] B. Bewer, M.Sc. Thesis: *"Development of a Gain Monitoring System for a Neutron Detector Array"*, University of Saskatchewan, 2005.

[Bir64] J.B. Birks, *The Theory and Practice of Scintillation Counting*, Pergamon Press, New York, 1964.

[Bla07] M. Blackston, Ph.D. Thesis: *"Precision Measurements of Deuteron Photodisintegration using Linearly Polarized Photons of 14 and 16 MeV"*, Duke University, 2007.

[Cha08] D. Chabot, M.Sc. Thesis: *"A PC-Based Data Acquisition System for Sub-Atomic Physics Measurements"*, University of Saskatchewan, 2008.

[GEA03] GEANT4 Collaboration, *Nucl. Inst. and Meth., Section A, Vol. 502, Issues 2-3,* 2003, Pages 666-668; GEANT4 Collaboration, *IEEE Trans. Nucl. Sci. NS-53,* 2006, 270.

[Gro00] D. E. Groom et al., *The European Physical Journal, C15, Issues 1-4,* 2000.

[Hir06] K. Hirose et. al., *Nucl. Inst. and Meth., Section A, Vol. 564, Issue 1*, 2006, Pages 100-107.

[Kir00] A.S. Kirov, W. R. Binns et al, *Nuclear Instruments and Methods in Physics Research, Section A, Vol. 439, Issue 1,* 2000, Pages 178-188.

[Kno00] G.F. Knoll, *Radiation Detection and Measurement*, 3rd Edition, John Wiley & Sons, 2000.

[Leo94] W.R. Leo, *Techniques for Nuclear and Particle Physics Experiments*, Second Revised Edition, Springer-Verlag, Berlin, 1994.

[Mur95] D. Murray, G. Wright and A. Wilson, *LUCID User's Guide*, 1995.

[Pru62] J.S. Pruitt and S.R. Domen, *"Determination of Total X-Ray Beam Energy with a Calibrated Ionization Chamber"*, National Bureau of Standards Monograph 48, 1962.

[Pyw06] R.E. Pywell, B.D. Sawatzky, J. Ives, N.R. Kolb, R. Igarashi and W.A. Wurtz**,** *"Light output response of BC-505 liquid scintillator", Nucl. Inst. and Meth., Section A, Vol. 565*, *Issue 2,* 2006, Pages 725-730.

[Pyw09] R.E. Pywell, O. Mavrichi, W.A. Wurtz and R. Wilson, *"Photon flux monitor for a mono-energetic gamma ray source", Nucl. Inst. And Meth., Section A, Vol. 606*, *Issue 3,* 2009, Pages 517-522.

[Reg03] T. Regier, M.Sc. Thesis: *"Development of a Gamma-Ray Beam Profile Monitor for the High-Intensity Gamma-Ray Source"*, University of Saskatchewan, 2003.

[Rey02] R. Reynolds, *APS Meeting Abstracts*, DNP5P1061R, 2002.

[Saw05] B. Sawatzky, Ph.D. Thesis: *"A measurement of the neutron asymmetry in d(γ, n)p near threshold"*, University of Virginia, 2005.

[Sob06] D.I. Sober et. al., *Nucl. Inst. and Meth., Section A, Vol. 440, Issue 2*, 2000, Pages 263-284.

[Vas96] V.G. Vasil'chenko et al., *Nucl. Instrum. Meth., Section A, Vol. 369, 55,* 1996.

[Vog93] J.M. Vogt, R.E. Pywell, D.M. Skopik, E.L. Hallin, J.C. Bergstrom, H.S. Caplan, K.I. Blomqvist, W. Del Bianco, and J.W. Jury, *Nucl. Inst. And Meth., Section A, Vol. 324*, 1993, Pages 198-208.

[Wel03] H.R. Weller, M.W. Ahmed*, "The HIGS facility: A free-electron laser generated gamma-ray beam for nuclear physics", Modern Physics Letters A, Vol. 18, No. 23,* 2003, Pages 1569-1590.

[Wil91] W.S.C. Williams, *Nuclear and Particle Physics*, Clarendon Press, Oxford, 1991.

[Yam77] M. Yamashita, *Nucl. Instrum. Meth., Vol. 142*, 1977, Pages 435-437.